

Iron Complexes of a Proton-Responsive SCS Pincer

Ligand with Sensitive Electronic Structure

Kazimer L. Skubi,^{†,a} Reagan X. Hooper,^{†,a} Brandon Q. Mercado,^a Melissa M. Bollmeyer,^b

Samantha N. MacMillan,^b Kyle M. Lancaster,^b Patrick L. Holland^{,a}*

^a Department of Chemistry, Yale University, New Haven, Connecticut 06511.

^b Department of Chemistry and Chemical Biology, Cornell University, Ithaca, New York 14853.

[†] These authors contributed equally, and should be considered co-first authors.

Abstract: SCS pincer ligands have an interesting combination of strong-field and weak-field donors that is also present in the nitrogenase active site. Here, we explore the electronic structures of iron(II) and iron(III) complexes with such a pincer ligand, bearing a monodentate phosphine, thiolate S donor, amide N donor, ammonia, or CO. The ligand scaffold features a proton-responsive thioamide site, and the protonation state of the ligand greatly influences the reduction potential of iron in the phosphine complex. The N–H bond dissociation free energy can be quantitated as 56 ± 2 kcal/mol. EPR spectroscopy and SQUID magnetometry measurements show that the iron(III) complexes with S and N as the fourth donors have an intermediate spin ($S = 3/2$) ground state with large zero field splitting, and X-ray absorption spectra show high Fe–S covalency. The Mössbauer spectrum changes drastically with the position of a nearby alkali metal cation in the iron(III) amido complex, and DFT calculations explain this phenomenon through a change between having the doubly-occupied orbital as d_{z^2} or d_{yz} , as the former is more influenced by the nearby positive charge.

INTRODUCTION

The organometallic chemistry of iron has been dominated by strong-field supporting ligands such as CO, CN, and phosphines, and by macrocyclic N ligands like porphyrins.¹⁻⁶ The active sites of hydrogenase enzymes incorporate S-based ligands, and these are low-spin due to the influence of carbonyl and cyanide donors.⁷ However, the interesting reactions of nitrogenase enzymes, and a new generation of low-valent iron catalysts, have predominantly weak-field ligands and have led to increasing interest in organometallic iron complexes with higher spin states.⁸⁻¹¹ We focus here on iron coordination environments that result from a mixture of C and S donors – choices that are particularly compelling since the six “belt” iron atoms in the iron-molybdenum cofactor (FeMoco) of nitrogenase have a mixed C/S coordination sphere.¹²⁻¹⁴ This unusual combination of potentially strong-field C donors and weak-field S donors could lead to changes in spin states during catalysis, which has been linked to changes in barriers and selectivity.¹⁵⁻¹⁸ Thus, the study of C- and S-ligated iron has relevance for both fundamental coordination chemistry and bioinorganic mechanisms.¹⁹⁻²¹ However, CO-free iron complexes with supporting ligands that coordinate through only carbon and sulfur donors are rare.²²⁻²⁸ Of these examples, only one multidentate C/S ligand is known to support N₂ binding.²⁶ In addition, Qu has provided important studies on Cp*-supported iron dimers bridged by dithiolates, and this C/S ligand sphere can bind and facilitate the reduction of nitrogenase-relevant N_xH_y substrates.^{23-25, 29}

Our group's recent work on SCS systems began with a dithiolate ligand having a central arene that can interact with iron through backbonding into its π -system in low oxidation states.^{26, 30} While this hemilabile interaction stabilizes the reduced complexes, complete dissociation of the SCS ligand occurred in the presence of Brønsted acids, and backbonding into N₂ competed with backbonding into the arene. In order to address this instability, we then moved to tridentate pincer

scaffolds in which the carbon forms a σ -bond to the iron center. Namely, we synthesized a new SCS pincer comprised of an *N*-heterocyclic carbene (NHC) ligand with two bulky thiolate arms, and isolated a number of iron complexes with this scaffold.²⁸ The geometries at iron sites with this supporting ligand were sometimes tetrahedral and sometimes square planar, indicating significant flexibility in the core. However, this NHC ligand was also sensitive to acids, and the ligand synthesis involved time-consuming protection and deprotection steps.

Here, we study the first iron complexes of pincer ligands containing a central aryl C donor and two S-donor arms. SCS pincers of this type have been studied in complexes of group 10 metals (Chart 1, top), but not in group 8 metals to our knowledge.³¹⁻³⁶ Thioamide arms are compelling, because they are easily prepared from readily available precursors and offer the potential for proton responsiveness.³⁷⁻³⁹ There is no precedent for iron complexes with thioamide-aryl ligands, although there is a related iron SNS pincer complex with a central pyridine (Chart 1, lower left).⁴⁰⁻

41

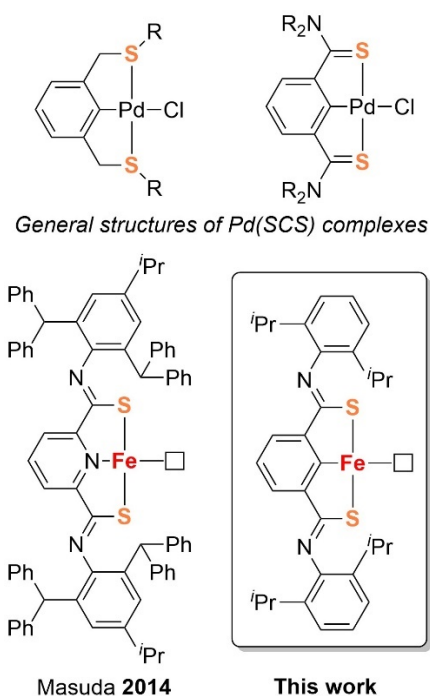


Chart 1. Typical palladium SCS pincer complexes and closely-related iron complexes with SNS and SCS pincers. In the bottom pictures, the square represents a coordination site with various ligands.

Thioamides have two tautomers, which form the same anion upon deprotonation (Figure 1, right). Most often, the thioamide coordinates as an iminothiolate through the S donor rather than the potential N donor as a result of the relative weakness of the C=S π bond and the better overlap of the S atom with metal orbitals.⁴² After coordination, protonation at the N atom gives a formally neutral thione donor that maintains the M–S interaction (Figure 1, brackets). Even as a formally neutral ligand, the thione C–S bond is significantly polarized toward a $C^{\delta+}$ – $S^{\delta-}$ form that affords some anionic character at S.⁴³ The ability to tune the donor properties of iron-coordinated sulfur via protonation/deprotonation of the supporting ligand could be used to probe how protonation state can affect the redox potential, spectroscopic characteristics, and reactivity of the iron center.

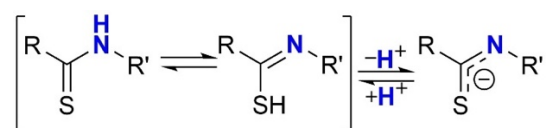


Figure 1. Illustration of thioamide tautomerization and deprotonation to form an anionic donor.

The potential for proton responsiveness is also relevant to nitrogenase mechanisms. The Thorneley-Lowe kinetic scheme for nitrogenases proposes that one proton is transferred to the FeMoco with each reduction step,⁴⁴ but the location of these protons has been controversial. Computational studies have showed that there are many potential sites of protonation on the FeMoco, including the sulfides,⁴⁵⁻⁴⁸ the Mo-coordinated homocitrate,^{46, 49} and even the carbide.⁴⁷⁻

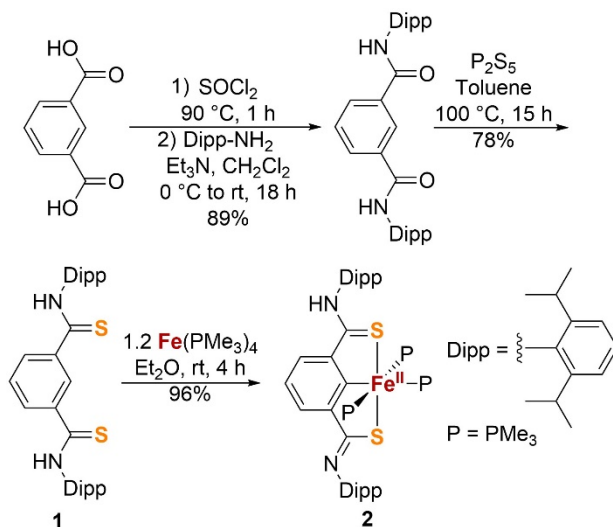
^{48, 50} Studies on multi-site proton-coupled electron transfer (PCET) have demonstrated that various protonation sites can influence the redox potentials and bond dissociation free energies (BDFE).⁵¹⁻
⁵⁴ These inspirations motivated us to pursue thermochemical studies on well-characterized (SCS)Fe complexes with proton-responsive ligands to examine the effects of distant protonation events on potentially biologically-relevant iron sites.

In the present study, we describe a new ligand scaffold that incorporates thioamides and an anionic aryl group to mimic the sulfur and carbon coordination environment found in FeMoco. The ligand is easy to prepare on a useful scale, and the stability of the iron complexes is highlighted by the ability of an iron(III) complex to be handled in air and water. Although no iron complex of the new SCS ligand was observed to bind N₂, we use EPR and Mössbauer spectroscopy alongside magnetometry measurements to elucidate the unusual electronic structures of complexes with different exogenous donors, including biologically-relevant amide, thiolate, ammonia, and CO. In the amide complex, the electronic structure may be influenced to the presence of nearby cations. We also demonstrate the ability of the thioamide arm to be proton responsive, and quantify the connection between protonation state and redox state of iron.

RESULTS

Ligand Synthesis and Metalation. Using a procedure modified from the literature,⁵⁵ isophthalic acid was treated with thionyl chloride followed by 2,6-diisopropylaniline, which provided the diamide (Scheme 1). Reaction of this compound with P₂S₅ in toluene at 100 °C yielded the bis(thioamide) **1**, in an overall yield of 69% in two steps from commercial starting materials. Treating **1** with a slight excess of Fe(PMe₃)₄ in Et₂O at room temperature led to

effervescence and a color change from yellow-brown to dark green, and iron complex **2** was isolated in 93% yield (Scheme 1).⁵⁶⁻⁵⁷



Scheme 1. Synthesis and metalation of SCS pincer ligand **1**. Dipp = 2,6-diisopropylphenyl.

Crystallization of **2** gave green blocks suitable for X-ray diffraction (Figure 2, top). The diffraction data showed an octahedral iron site with a meridional pincer ligand as expected. The Fe–C bond length is 1.9502(18) Å, and the average Fe–S length is 2.268(9) Å. The three Fe–P bonds are only slightly different, with a length of 2.2484(3) Å for the phosphine *trans* to C and lengths of 2.2553(4) Å and 2.2608(4) Å for the phosphines *cis* to C. There was disorder at the thioamide N–H site, which was satisfactorily modeled with each thioamide having 50% hydrogen atom occupancy, consistent with single protonation of the supporting ligand in **2**.

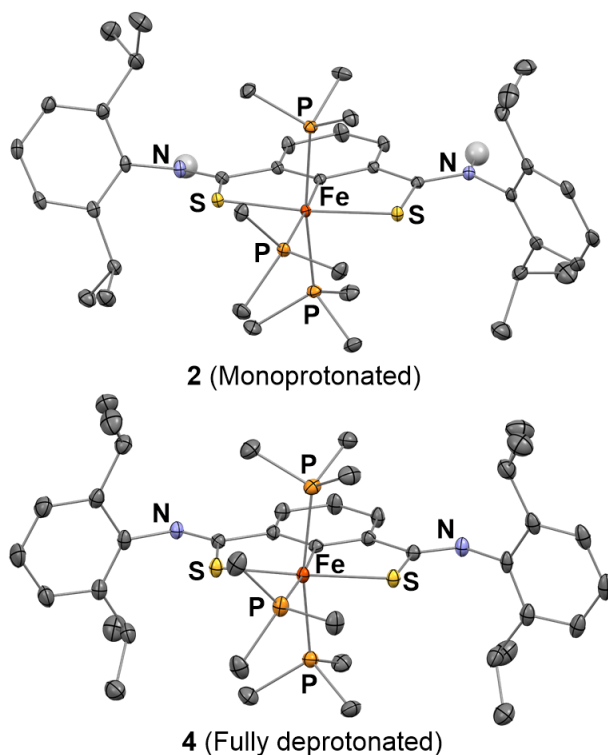


Figure 2. Molecular structures of monoprotonated iron(II) complex **2** and fully deprotonated iron(III) complex **4**, plotted as 50% probability thermal ellipsoids. All hydrogen atoms except those bonded to N are hidden for clarity, and each N–H site is modeled as having 50% hydrogen atom occupancy.

The Mössbauer spectrum of **2** has a doublet with $\delta = 0.21$ mm/s and $|\Delta E_Q| = 1.25$ mm/s (Figure S46). Proton NMR spectra in either C_6D_6 or $THF-d_8$ show signals in the range expected for a diamagnetic complex of low-spin iron(II). The most downfield resonance integrates 1:1 with proton groups from each side of the molecule (Figure S5). Adding D_2O made this signal disappear, and therefore it is assigned as the thioamide proton. Based on the NMR spectra, **2** is unsymmetric in solution, and it is best described as having one neutral thioamide S donor and one anionic iminothiolate donor. The solid-state IR spectrum of **2** shows a broad peak centered at 3336 cm^{-1} (Figure 3, red trace), which is distinct from the analogous signal in free ligand **1** at 3136 cm^{-1} .

(Figure 3, gray trace), consistent with an N–H stretching vibration. We hypothesize that the thioamide arm is deprotonated during the synthesis of **2** by a transient iron hydride to form H_2 , which explains the effervescence during metalation.

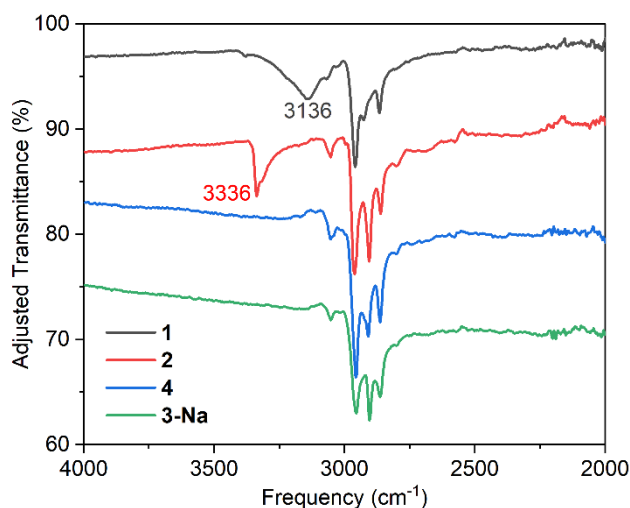


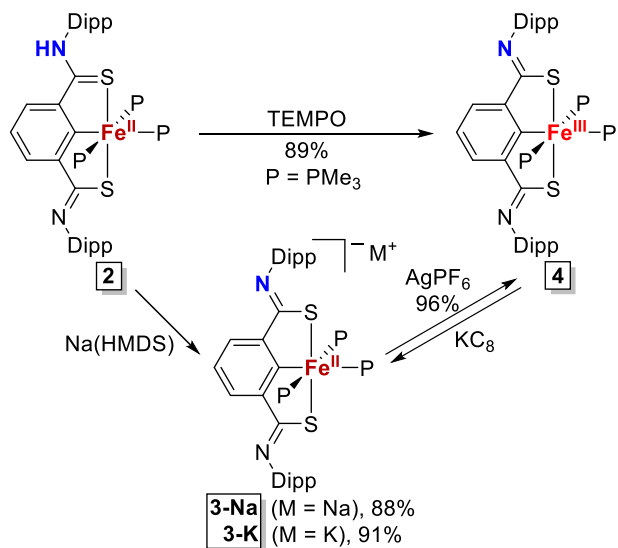
Figure 3. Solid state IR spectra of neutral ligand **1** and monoprotonated ferrous complex **2**, ferri-iminothiolate complex **4**, and ferrous iminothiolate complex **3-Na** in the range of 4000 to 2000 cm^{-1} . The bands assigned to N–H stretches (3136 and 3336 cm^{-1}) in the spectra of **1** and **2** are labeled.

Electron and Proton Transfer in Phosphine Complexes. We serendipitously discovered that neutral, fully-deprotonated iron(III) compound **4** could also be prepared in one pot from **1** and $Fe(PMe_3)_4$ by simply exposing the crude product **2** to air after metalation was complete. Proton NMR and UV-visible spectroscopy of air-exposed **2** *in situ* demonstrates rapid and complete conversion to **4**, with no monoprotonated iron(III) transient species observed. This one-pot procedure afforded **4** in 88% yield from **2**, and this method was used to prepare **4** for subsequent experiments. Additional proton and electron transfer reactions were carried out on **2** and **4**.

Treating the neutral iron(II) compound **2** with stoichiometric sodium bis(trimethylsilyl)amide provided anionic complex **3-Na**. Oxidation of **3-Na** using AgPF₆ afforded neutral iron(III) complex **4**. We generated the potassium analogue, **3-K**, by treatment of neutral iron(III) compound **4** with stoichiometric KC₈. Both have sharp peaks in their ¹H NMR spectra suggesting low-spin iron(II), and their structures were inferred based on these spectra (Figures S7 and S9). Their yields (88% for **3-Na** and 91% for **3-K**) were determined by integration relative to an internal standard. Alternatively, **4** could be formed in one step by hydrogen atom abstraction from **2** using TEMPO.

The X-ray crystal structure of the fully-deprotonated iron(III) complex **4** (Figure 2, bottom) shows an Fe–C bond length of 1.9413(12) Å, which is indistinguishable from the analogous distance in the monoprotonated iron(II) complex **2**. The average Fe–S length is 2.23(2) Å in **4**, which is slightly shorter than in **2**. Again, all three Fe–P bond distances are different, with the phosphine *trans* to C having the shortest bond of 2.2692(6) Å while the *cis* phosphines have lengths of 2.3007(6) Å and 2.3050(5) Å. The average Fe–P bond in **4** is shorter than in **2** (2.23(1) Å vs. 2.255(4) Å). Thus, there is a general contraction of bonds in ferric **4** when compared to ferrous **2**, consistent with **4** being more oxidized.

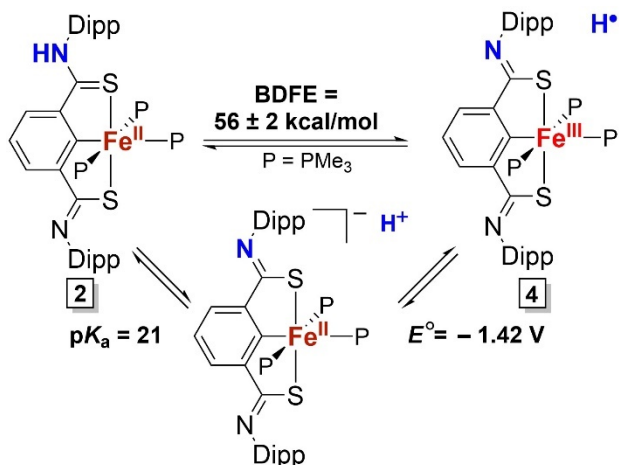
As expected for complexes lacking protonated thioamides, **3-Na** and **4** do not have any IR bands above 3050 cm⁻¹ that correspond to N–H stretching vibrations (Figure 3, blue and green traces). Proton NMR spectra of ferric **4** contain very broad peaks between –20 and +12 ppm (Figure S11), and the ³¹P NMR spectrum is featureless, as expected for nuclei directly bound to a paramagnetic metal. The relative integrations of the evident peaks in the ¹H NMR spectra of **3-M** in THF-*d*₈ are consistent with C_{2v} symmetry. Taken together, the IR and NMR data support double deprotonation of the thioamide groups of the supporting ligand in **3-Na** and **4**.



Scheme 2. Conversion of **2** to **4** using stepwise and concerted H atom removal. Yields were determined by ^1H NMR using an internal standard.

Cyclic voltammetry (CV) studies of **4** showed a reversible $\text{Fe}^{3+/2+}$ couple at $E_{1/2} = -1.42$ V vs. Fc^+/Fc in THF (Figure S60). The peak currents displayed a linear dependence on the square root of the scan rate, indicating that the process is diffusion controlled (Figure S61). Next, we tested the ability of different organic bases to deprotonate **2**, using changes in the ^{31}P NMR chemical shifts to determine the ratio of **2** and deprotonated **2** since the conjugate base and acid are in rapid equilibrium. We assumed that the chemical shifts from the ^{31}P NMR spectrum of **3-K** represent the shifts of fully-deprotonated **2**. Addition of neither Et_3N ($\text{p}K_{\text{aH}} = 12.5$ in THF) nor DBU ($\text{p}K_{\text{aH}} = 16.9$ in THF) gave changes in the NMR spectra of **2**.⁵⁸ An initial 1.10 equiv addition of triazabicyclodecene (TBD, $\text{p}K_{\text{aH}} = 21.0$ in THF)⁵⁸ equilibrated with **2**, on the other hand, gave a ^{31}P NMR spectrum with peaks at 12.1 ppm and 10.8 ppm. These shifts are 4.8 ppm upfield from the ^{31}P resonances of **3-K** but 1.4 ppm downfield of ^{31}P resonances of **2** (Figure S86). This result indicates that the $\text{p}K_{\text{a}}$ of **2** is 22 ± 1 in neat $\text{THF-}d_8$. An equivalent NMR experiment in 0.3 M

$[N^tBu_4][PF_6]$ in THF- d_8 (the electrolytic solution used for CV) indicated a pK_a of 21 ± 1 . (Figure S87) These data enable us to define the bond dissociation free energy (BDFE) of the N–H bond using the Bordwell equation, with $C_G(THF) = 60.4 \pm 2$ kcal/mol.⁵⁹⁻⁶⁰ This analysis gave a BDFE(N–H) of 56 ± 2 kcal/mol (Scheme 2).



Scheme 2. Thermodynamic values used to calculate the BDFE.

Other redox and protonation tests were used as well. Electrochemical oxidation of **2** is irreversible under the same CV conditions used for **4** (Figure S59). To test whether **4** could be protonated, it was treated with one equiv of $[H(OEt_2)_2][BF_4]$ in THF. A dark brown solid precipitated from the reaction mixture, and the IR spectrum of the solid showed a single N–H stretch at 3250 cm^{-1} , which is much lower than the N–H stretching frequency of **2** at 3336 cm^{-1} . (Figure S88). Though purification and subsequent electrochemical testing of the putative protonated **4** was prevented by its insolubility, the IR spectrum of acid-treated **4** may indicate the feasibility of thioamide protonation. This direction was not pursued further.

Spectroscopy of Phosphine Complexes. The Mössbauer signal for **2** ($\delta = 0.21$ mm/s and $|\Delta E_Q| = 1.25$ mm/s, Figure S46) is similar to those for **3-Na** ($\delta = 0.24$ mm/s and $|\Delta E_Q| = 0.94$ mm/s,

Figure S47) and **3-K** ($\delta = 0.25$ mm/s and $|\Delta E_Q| = 1.05$ mm/s, Figure S48), consistent with low-spin iron(II) complexes. Solid **4** has a lower isomer shift of 0.16 mm/s and much larger quadrupole splitting of 3.45 mm/s, and its doublets are highly asymmetric, with $\Gamma_L = 0.57$ mm/s, $\Gamma_R = 0.32$ mm/s. To determine the spin state of **4**, solid state and C₆D₆ solution magnetic moments were obtained. Both measurements gave $\mu_{\text{eff}} = 1.6 \mu_B$ at 298 K, which indicates a ground-state spin of $S = 1/2$.

Spectroscopy and DFT calculations using B3LYP/ZORA-def2-TZVP were further employed to reveal the electronic structure of **4**. The EPR spectrum of **4** in 2-methyltetrahydrofuran (MeTHF) at 77 K was modeled as an $S = 1/2$ spin system with $g = [2.200, 2.120, 1.998]$ and coupling to three ³¹P nuclei: two with $|A| = [71, 83, 71]$ MHz and one with $|A| = [0, 37, 37]$ MHz (Figure 4). Mulliken spin population analysis showed spin populations of -0.036 on the axial phosphorus atoms and -0.019 on the equatorial phosphorus, in agreement with the fit to two equivalent ³¹P nuclei having larger A than a third ³¹P nucleus. The spin population analysis also showed an averaged spin density of 0.031 on the two ligand nitrogen atoms, though the smaller nuclear magnetic moment of ¹⁴N relative to ³¹P likely contributed to smaller, unresolvable ¹⁴N hyperfine splitting, which was modeled by anisotropic H-strain of $[66, 27, 0]$ MHz in the simulation.

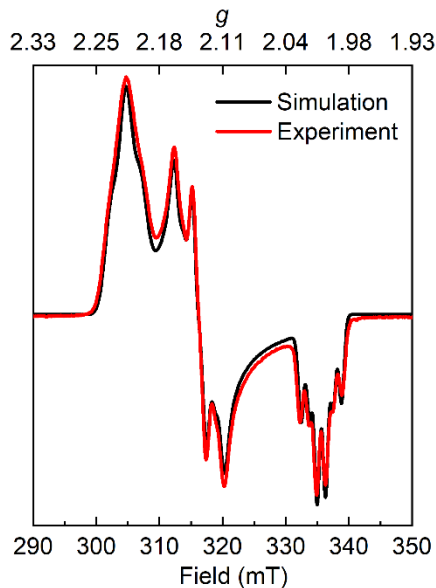
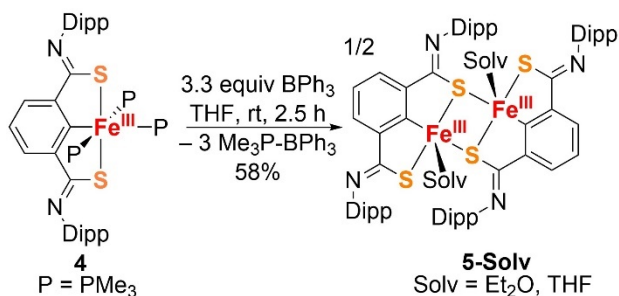


Figure 4. X-Band EPR spectrum of **4** at 77 K (1.0 mM in 2-MeTHF) measured with a microwave frequency of 9.384 GHz and power of 1.779 mW. Parameters for simulation: $g_1 = 2.200$, $|A_1(^{31}\text{P})| = 71, 71, 0$ MHz; $g_2 = 2.120$, $|A_2(^{31}\text{P})| = 83, 83, 37$ MHz; $g_3 = 1.998$, $|A_3(^{31}\text{P})| = 71, 71, 37$ MHz; $\text{HStrain} = [66, 27, 0]$ MHz.

Synthesis of Phosphine-Free SCS Iron Complexes. We next investigated the feasibility of removing the phosphine ligands. When iron(III) species **4** was treated with a slight excess of triphenylborane in THF, the color of the reaction mixture changed from green to orange, and precipitation of $\text{Me}_3\text{P-BPh}_3$ was observed (Scheme 3). Crystallization from Et_2O gave **5-Et₂O** in 58% yield (Figure S70). Dissolving **5-Et₂O** in THF and removing solvent under vacuum several times led to the formation of **5-THF** (Figure S69). We refer to these compounds collectively as **5-Solv** because of their similarity and ability to interconvert as a function of solvent.



Scheme 3. Phosphine abstraction with triphenylborane. Dipp = 2,6-diisopropylphenyl.

Both compounds **5-Solv** are dimeric in the solid state (Figure 5), with each iron center in a square pyramidal geometry with a coordinated solvent molecule occupying the axial site. The dimers adopt a butterfly shape in which the two iron centers are bridged by one sulfur from each ligand. In **5-Et₂O**, the planes containing each pincer intersect at 75°. Comparing the two arms of the pincer ligand in **5-Et₂O**, the bridging Fe–S bond is longer than the non-bridging Fe–S by 0.08 Å. Other bond metrics of **5-Et₂O** are comparable to those in phosphine precursor **4**, and the long C–S (1.78(3) Å average) and short C–N bonds (1.26(1) Å average) indicate two anionic iminothiolate donors. The metrical parameters of **5-THF** are nearly identical to those of **5-Et₂O**, with Fe–C bond lengths of 1.961(2) Å (**5-THF**) and 1.966(3) Å (**5-Et₂O**), Fe–S_{bridging} bond lengths of 2.2557(7) Å (**5-THF**) and 2.278(1) Å (**5-Et₂O**), and Fe–S_{non-bridging} bond lengths of 2.1797(7) Å (**5-THF**) and 2.187(1) Å (**5-Et₂O**).

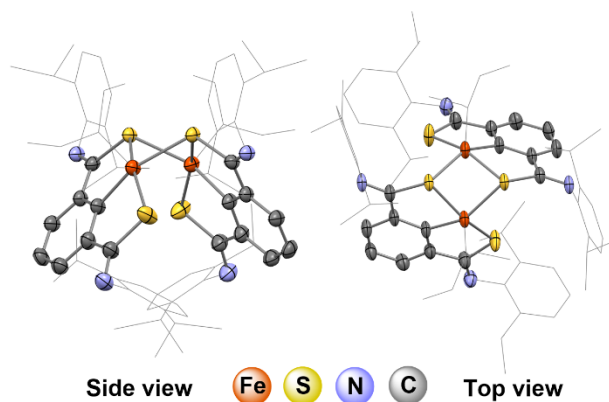


Figure 5. Molecular structure of **5-Et₂O** plotted at 50% probability thermal ellipsoids, showing its dimeric butterfly shape from side and top views. Dipp groups and Et₂O are shown in wireframe.

Mössbauer spectra of solid **5-Et₂O** and **5-THF** are also comparable, with parameters of $\delta = 0.34$ mm/s and $|\Delta E_Q| = 3.91$ mm/s for **5-Et₂O** and $\delta = 0.34$ mm/s, $|\Delta E_Q| = 3.73$ mm/s for **5-THF** (Figures S50 and S51). Mössbauer spectra of **5-THF** differ, however, between the solid state and a frozen THF solution. Specifically, there is a higher isomer shift of 0.45 mm/s for the frozen-solution spectrum, which may suggest that the dimer is broken up with THF replacing the bridging sulfur (Figure S89). The frozen solution also shows an increased quadrupole splitting and marked doublet asymmetry ($|\Delta E_Q| = 4.26$ mm/s, $\Gamma_L = 0.73$ mm/s, $\Gamma_R = 0.49$ mm/s). The ¹H NMR spectrum of **5-Et₂O** in THF-*d*₈ shows six broad signals between 12 and −81 ppm (Figure S12). The number and integration of the peaks is consistent with *C*_{2v} symmetry; a seventh expected peak integrating to 4H was not resolved, likely due to broadening. This is also consistent with the dimer breaking up, although it is also possible that there is some other dynamic phenomenon. The ¹H NMR spectra of **5-Solv** in C₆D₆ have at least 12 peaks with considerable broadness, which prevented further analysis but points to a lowered symmetry in the dimer.

Cyclic voltammetry of **5** showed three irreversible reduction events (Figure S62). An attempt to reference the reduction potentials to a ferrocene internal standard was unsuccessful due to reactivity with Fc and Fc⁺. The lack of electrochemical reversibility may be due to large structural changes occurring different oxidation states. Undeterred, we proceeded to stoichiometrically reduce **5** with 1 equiv of KC₈ per iron at −78 °C in THF, which resulted in a deep purple solution. Crystallization from diethyl ether at −40 °C give iron(II) complex **6** in 46% yield. Its X-ray crystal structure, shown in Figure 6, shows a tetrameric assembly in the solid state, with K⁺ bridging S atoms and Dipp groups. There are six (SCS)Fe units in each asymmetric unit, and the average Fe–C and Fe–S_{Pincer} bond lengths are 1.947(4) Å and 2.23(9) Å, respectively. The average distance between S and K in the central bridge is 3.19(1) Å. As in **5-Solv**, the Fe–S bond lengths are ~0.05 Å longer on the side of the pincer where the S is bridging two iron centers. Complex **6** is extremely air sensitive and decomposes in solution over a few days.

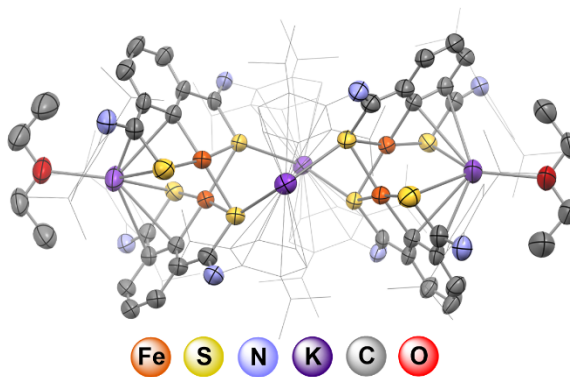
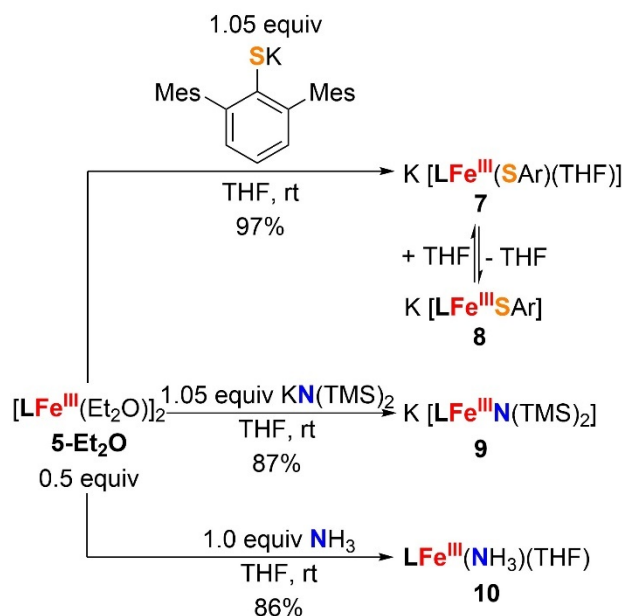


Figure 6. Molecular structure of **6**. Thermal ellipsoids are displayed at the 50% probability level. Dipp groups are shown in wireframe and hydrogen atoms are omitted. Two-thirds of the asymmetric unit is shown.

The ^1H NMR spectrum of **6** in $\text{THF-}d_8$ shows at least 19 resonances between -50 and $+15$ ppm, reflecting C_1 symmetry in solution. We were unable to assign resonances to specific proton environments due to peak broadness and overlapping in the 0 to 8 ppm region (Figure S13). Despite the complexity of the ^1H NMR spectrum and crystal structure, the solid-state Mössbauer spectrum of **6** (Figure S52) has a single quadrupole doublet with an isomer shift similar to that of the starting material (0.34 mm/s for **6** vs. 0.35 mm/s for **5-Et₂O**), but a smaller quadrupole splitting (1.87 mm/s for **6** vs. 3.91 mm/s for **5-Et₂O**). The Mössbauer spectrum suggests that all iron sites are equivalent.

Next, we sought to test **6** for the ability to bind N_2 at low temperatures using variable-temperature UV-visible spectroscopy. Negligible spectral changes were observed between 25 and -100 °C in THF, Et_2O , or toluene (Figure S90a-S90c). Addition of stoichiometric amounts of 18-crown-6 slightly shifted the absorption maxima, but the resulting species also did not exhibit notable temperature-dependent spectral changes (Figure S90d-S90f). Thus, it does not appear that **6** undergoes speciation changes or N_2 binding at these concentrations and temperatures. Further reduction of the iron(II) tetramer **6** led to a silent NMR spectrum and a broad, featureless UV-Vis spectrum. The products formed in this reaction are unknown, and attempts to isolate or identify the species present were unsuccessful.

Synthesis of Monomeric Iron Complexes With S and N Donors. To study monomeric complexes of our SCS iron framework in the absence of strong phosphine donors, we next treated **5-Et₂O** with ligands containing S and N donors, which gave the products in Scheme 4 within 1 hour at room temperature. Their syntheses, NMR spectra, and IR spectra are described here, and their magnetism, EPR spectra and electronic structures are described in following sections.



Scheme 4. Synthesis of complexes **7–10**. L = triply deprotonated trianionic ligand **1**; Ar = 2,6-dimesitylphenyl.

Addition of a bulky thiolate (potassium 2,6-dimesitylphenylthiolate) to **5-Et₂O** in THF generated complex **7** in 97% yield. Addition of 18-crown-6 followed by crystallization furnished **7-crown** (Figure S81). **7-Crown** displays an axially coordinated THF molecule and a nearly square pyramidal geometry with $\tau_5 = 0.08$ (Figure S81). The Fe–C, average Fe–S_{Pincer}, and Fe–S_{Ar}, bond lengths are 2.0006(17) Å, 2.244(6) Å, and 2.2758(5) Å, respectively. Addition of Et₂O, arenes, or alkanes to solid **7** prior to the addition of 18-crown-6 led to a color change from orange to green, indicating the formation of the THF-free analogue (**8**) in non-coordinating solvents. Compound **8** was crystallized from toluene in the presence of 18-crown-6 as **8-crown** (Figure 7, top, and Figure S82). The geometry is distorted from square planar, with $\tau_4 = 0.20$. The Fe–S_{Ar} bond distance is 2.2448(8) Å, which is shorter than the Fe–S_{Ar} bond in **7-crown** (Table 1). Unlike the structure of the THF adduct **7-crown**, one mesityl group of THF-free **8-crown** is twisted to cover an axial iron site; however, the long 3.06 Å distance between iron and the arene centroid is

inconsistent with a direct electronic interaction. We previously observed a similar orientation of this thiolate ligand in another SCS iron complex and ascribed this phenomenon to crystal packing effects.²⁸ We were unable to crystallize four-coordinate thiolate **8** without crown ether. The ¹H NMR spectrum of **8** in THF-*d*₈ has ten broad peaks between 15 and –63 ppm (Figure S14). Upon dissolution in THF-*d*₈, the color of **8** changes from dark brown to red, indicating that the THF-adduct **7** is likely formed. The number and integration of the signals suggests *C*_{2v} symmetry, which implies that the crystallographically observed lack of symmetry caused by the bulky aryl thiolate is not preserved in THF-*d*₈ solution.

Amide complex **9** was synthesized in 87% yield by treating **5** with KN(TMS)₂, and it was crystallized with and without 18-crown-6 to give structures of **9-crown** (Figure S84) and **9** (Scheme 4, middle, and Figure S83), respectively. Crown-free **9** is unstable as a solid at room temperature and in solution even at –40 °C, as evidenced by the appearance of multiple new peaks between 11 and –43 ppm in its NMR spectrum after a few days (Figure S17). Once this unknown impurity formed, we have been unable to remove it by recrystallization or washing. **9-Crown**, however, is more stable. The crystallographic structures of **9** and **9-crown** lack axial solvent coordination (despite **9** being crystallized from THF), and their color is the same in coordinating and non-coordinating solvents. These observations suggest that solvent coordination to the N(TMS)₂ adduct is unfavorable, possibly because the TMS groups block the axial sites.

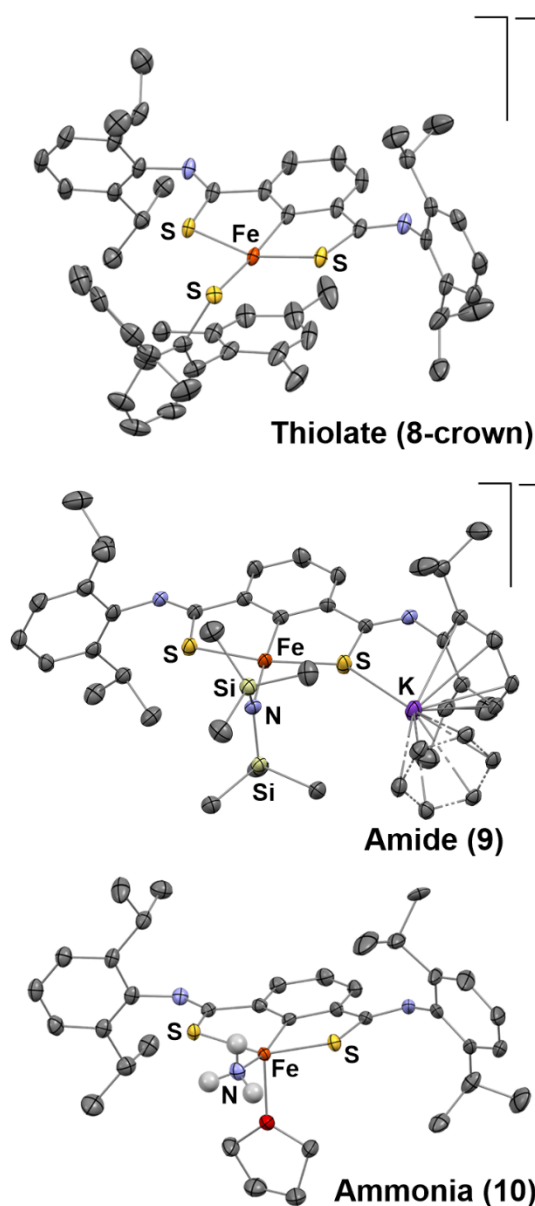


Figure 7. Molecular structures of **8-crown**, **9**, and **10** at 50% probability thermal ellipsoids.

Hydrogen atoms are excluded for clarity, with exception of the NH₃ hydrogen atoms of **10**. The outer-sphere potassium ion in **8-crown** is not shown.

The crystallographic structure of **9** displays a square planar molecular geometry at iron with $\tau_4 = 0.09$ - 0.11 . Fe–N bond lengths in **9** are Fe1–N14 = 1.915(3) and Fe2–N18 = 1.899(3),

which are distinguishable. Interestingly, the structure of **9** shows a potassium cation lying in the pincer plane, with a K1–S11 distance of 3.133(1) Å and K2–S15 distance of 3.126(1) Å. The Fe–S bond lengths on the side with potassium are 2.2459(9) Å (Fe1) and 2.2463(9) Å (Fe2), which are indistinguishable. The Fe–S bond length is, however, significantly shorter on the side of the molecule without the close S–K contact, with a difference of 0.0065(12) Å at Fe1 and 0.0080(12) Å at Fe2. Metrical parameters for **9-crown** are shown in Table 1. The ¹H NMR spectra of **9** and **9-crown** in THF-*d*₈ have eight and nine, respectively, paramagnetically-shifted peaks between 19 and –68 ppm (Figures S16 and S17), consistent with *C*_{2v} symmetry. Their chemical shifts are nearly the same.

Treating **5** with 1 equiv of NH₃ gas in THF furnished ammine complex **10** in 86% yield (Scheme 4, bottom). In the crystallographic structure, there are two molecules of **10** in the asymmetric unit, and each has an axially-coordinated THF that gives a distorted square pyramidal geometry with $\tau_5 = 0.09$ –0.14. The Fe–N bond lengths are 2.084(3) Å (Fe1) and 2.065(3) Å (Fe2). The molecule containing Fe2 shows a hydrogen bond between one NH₃ proton and one uncoordinated THF. Hence, the shorter Fe–N length in Fe2 may be due to the hydrogen bond, which increases the basicity of the NH₃. While the Fe–S bond lengths of **10** are similar to those in **8-crown** and **9-crown**, the Fe–C bond length is significantly shorter in **10** (Table 1). This difference may arise because the thiolate and amido ligands exert a larger *trans* influence than the ammine.^{61,62} The solid-state IR spectrum of **10** shows four weak bands at 3352, 3299, 3236, and 3159 cm^{–1} that are assigned as N–H stretches (Figure S44). Their frequencies are not suggestive of any significant coordination-induced N–H bond weakening. The ¹H NMR spectrum of **10** in THF-*d*₈ has nine resonances between 175 ppm and –78 ppm, consistent with *C*_{2v} symmetry (Figure S19). Since the complex is *C*_s symmetric with THF coordination on one face, the spectrum in THF-

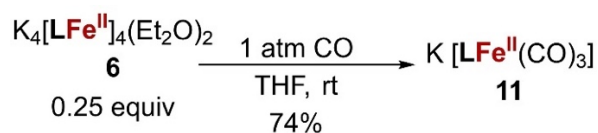
d_8 could indicate fast THF exchange on both sides of the complex. Its spectrum in C_6D_6 has severe broadening compared to THF- d_8 , and there are at least 15 resonances (Figure S20). Assuming that coordinated THF has two different proton environments and that NH_3 rotation on the NMR timescale renders its protons equivalent, a C_s symmetric geometry (with the mirror plane perpendicular to the pincer) would predict 14 peaks. Thus, the number of peaks in the C_6D_6 -solvated NMR spectrum suggests **10** has no symmetry in C_6D_6 , though the reason for the low symmetry is not obvious.

Table 1. Comparison of Fe–C, Fe–S, and Fe–X (X = SAr, N(TMS)₂, NH₃) bond lengths (in Å) in **7-crown**, **8-crown**, **9-crown**, and **10**. Ar = 2,6-dimesitylphenyl. Two sets of lengths for one parameter represent the two molecules in the unit cell.

Complex	Exogenous Ligand (X)	Fe–C	Average Fe–S _{Pincer}	Fe–X
7-crown	SAr	2.0006(17)	2.244(6)	2.2758(5)
8-crown	SAr	1.999(3)	2.250(5)	2.2448(8)
9-crown	N(TMS) ₂	2.002(6)	2.234(5)	1.882(5)
		2.010(5)	2.241(7)	1.902(4)
10	NH ₃	1.973(3)	2.24(1)	2.065(3)
		1.971(3)	2.25(1)	2.084(3)

Synthesis and Characterization of an Iron(II) Carbonyl Complex. Treating a THF solution of iron(III) complex **5** with 1 atm of CO gave little reaction, with 85% unreacted **5** remaining after 2 hours at room temperature, as judged by NMR spectroscopy. In contrast, stirring iron(II) complex **6** under 1 atm of CO afforded **11** in 79% yield after 1 hour (Scheme 5). Though crystallization attempts were unsuccessful, analytically pure material was isolated by removing THF under vacuum and washing the pale-yellow solids with Et₂O. Material generated in this way gave a Mössbauer spectrum with a quadrupole doublet at $\delta = 0.01$ mm/s and $| \Delta E_Q | = 0.99$ mm/s

(Figure S58). Low isomer shifts such as that of **11** are frequently observed in iron carbonyl complexes, reflecting the withdrawal of d-electron density from the iron nucleus by backbonding.⁶³ The ¹H and ¹³C NMR spectra of **11** show 7 and 14 narrow peaks, respectively (Figures S21 and S22). These spectra are consistent with a C_{2v}-symmetric diamagnetic species. The two most-downfield ¹³C signals have a relative integration of 2:1 and are assigned to the CO ligands. They have comparable chemical shifts to the CO signals in an SNS-supported iron(II) tricarbonyl complex.⁴⁰



Scheme 5. Synthesis of tricarbonyl complex **11**. L = triply deprotonated trianionic ligand **1**; Ar = 2,6-dimesitylphenyl.

The solid-state IR spectrum of **11** shows three bands in the region expected for CO stretching at 2078, 2013, and 1988 cm⁻¹ (Figure 8 and S45). To compare our experimental spectrum with theoretical IR spectra of SCS-supported complexes with either two or three CO ligands, we used DFT calculations (BP86/ZORA-def2-TZVP) to optimize and predict the CO stretching frequencies of [LFe(CO)₂]⁻ and [LFe(CO)₃]⁻. The model with two CO ligands predicted two IR-active bands of equal intensity, while the model with three CO ligands predicted stretching frequencies whose number and relative intensities matched the experimental spectrum (Figures S93 and S94). Thus, we assign the bands at 2078, 2013, and 1988 cm⁻¹ to CO stretching vibrations in an octahedral tricarbonyl complex.

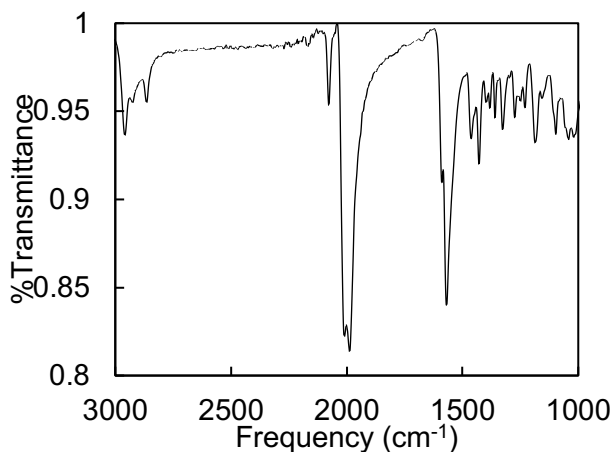


Figure 8. Solid state IR spectrum of **11** showing bands at 2078, 2013, and 1988 cm^{-1} that are assigned as CO stretches.

In an effort to produce complexes with fewer CO ligands, we treated **6** with substoichiometric CO. This treatment gave solutions with ^1H NMR spectra showing a large number of peaks with chemical shifts indicative of multiple paramagnetic species. Though we were unable to isolate any of these species, the mixture converted to diamagnetic **11** upon addition of greater than three equiv of CO (Figure S91).

X-Ray Absorption Spectra of Thiolate Complex 8. To gain insight into the Fe-S bonding in **8-crown**, which has iron(III) in the most biomimetic S_3C coordination sphere, Fe K-edge X-ray absorption spectra were measured. The spectrum showed two pre-edge features at ca. 7112 and 7114 eV. TD-DFT calculations reproduced the pre-edge features of the experimental spectrum (Figure 9, bottom). Frontier quasi-restricted orbital (QRO) analysis showed three singly-occupied orbitals of primarily Fe 3d character with $< 10\%$ S 3p mixing and a LUMO composed of 39.3% Fe 3d character and 21.3% S 3p character (Figure 9, top). The greater covalency between the Fe and S ligands in the LUMO is responsible for its increased energy. Based on the QRO analysis, the first pre-edge feature at 7112 eV is assigned to excitations of Fe 1s electrons into the three

nearly-degenerate singly-occupied orbitals, while the second feature at 7114 eV is assigned to an Fe 1s to LUMO excitation. As expected for iron in the +3 oxidation state, the large contributions of ligand S orbitals to the frontier QROs indicate a large degree of Fe-S bond covalency.

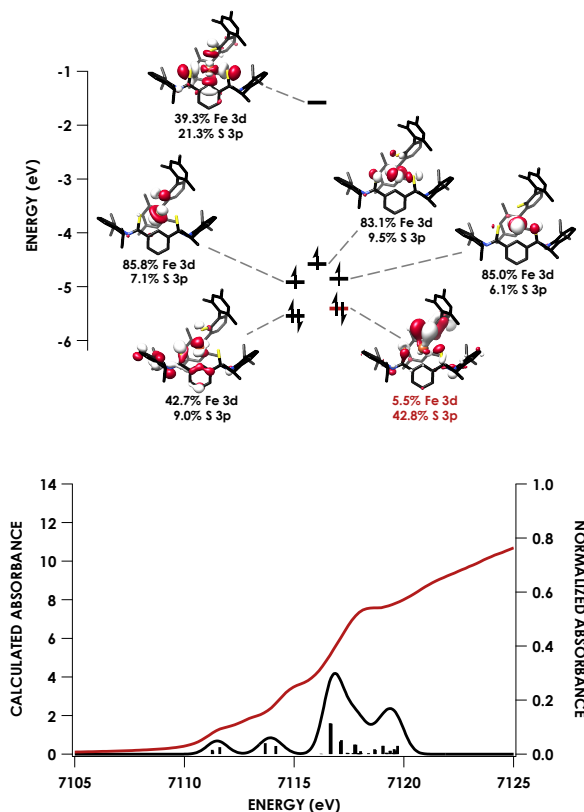


Figure 9. Top: Frontier MO diagram of **8**. Energies were obtained from the QROs (calculated using the B3LYP level of theory with the CP(PPP) basis set on Pd and ZORA-def2-TZVP(-f) on all other atoms). Ligand orbitals are labeled in red. Orbitals are plotted at an isovalue of 0.03 au with hydrogen atoms removed for clarity. Bottom: Overlay of the experimental (red) and TD-DFT calculated (black) Fe K-edge spectra for 8-crown. Black sticks represent individual transitions. The calculation employed the CP(PPP) basis set for Fe and the ZORA-def2-TZVP(-f) basis set for all other atoms.

Electronic Structures of S and N Donor Complexes from Magnetometry and EPR

Spectroscopy. The solution magnetic moments of the iron(III) complexes were measured at 298 K in THF-*d*₈, giving $\mu_{\text{eff}}(\mathbf{7}/\mathbf{8}) = 4.0 \pm 0.1 \mu_{\text{B}}$, $\mu_{\text{eff}}(\mathbf{9}) = 4.1 \pm 0.1 \mu_{\text{B}}$, and $\mu_{\text{eff}}(\mathbf{10}) = 4.1 \pm 0.1 \mu_{\text{B}}$. These moments are consistent with a well-isolated $S = 3/2$ ground state. Note that in THF solution, thiolate complex **8** is in equilibrium with its THF adduct **7**. At 298 K, the solid-state magnetic susceptibilities of **8**, **9**, and **10** show χ_{MT} of 1.4, 2.3, and 1.9 cm³ K mol⁻¹, respectively, under a 5000 Oe applied field. These values are also consistent with an $S = 3/2$ ground state and little mixing of excited states (Figures S63-S65). To further evaluate the zero-field splitting (ZFS) parameters, we measured the low-temperature solution X-band EPR spectra in MeTHF and magnetization curves at ≤ 10 K under field strengths of 1 T to 7 T. The data were fit within the constraints of the usual spin Hamiltonian for an $S = 3/2$ spin system.

Variable-temperature (3 K to 10 K) magnetization data of thiolate complex **8** showed nesting of curves obtained at different fields, with saturation around $1.6 \mu_{\text{B}}$ (Figure S66, top). These data were fit to $g = [2.30, 2.30, 1.89]$ ($g_{\text{iso}} = 2.16$) and $D = -28(1) \text{ cm}^{-1}$; an adequate fit could not be obtained with positive D . At 10 K, complex **8** has an extremely broad EPR spectrum with poorly-resolved signals at $g \approx 5.7, 5.2, 4.5, 4.3, 2.2, 2.1$, and 1.2 as well as sharp signals at $g = 2.02, 2.03$, and 2.00 (Figure 10, top). The sharp set of signals near $g = 2.00$ is assigned to a $S = 1/2$ impurity (1%) with $g = [2.08, 2.03, 2.00]$. An acceptable simulation of the remainder of the EPR spectrum was obtained using $S = 3/2$, g and D values derived from the magnetization data, and E/D of 0.20. D strain of 28 cm^{-1} (100% of D) was required to account for the broad spectrum. The necessity of large D strain to capture the overall shape of the spectrum indicates that a wide distribution of ZFS parameters were sampled in the spectrum. EPR spectra with similarly strain-dominated line shapes have been observed for other $S = 3/2$ iron complexes.^{64,65} In our system,

the crystallographically-observed flexibility of the thiolate ligand may result in a mixture of conformers with varying ZFS. Based on the range of observed g values, the range of E/D for different conformers of **8** present in MeTHF is estimated to be between 0.1 and 0.2.

Isofield lines from 2 to 10 K for amide complex **9** also show a field dependence, with saturation near $2.0 \mu_B$. These magnetization curves were fit to $g = [2.15, 2.54, 2.33]$ ($g_{\text{iso}} = 2.34$) and $D = -30(2) \text{ cm}^{-1}$ (Figure S66, middle). No reasonable fit was found using $D > 0$. The 5 K EPR spectrum shows a sharp, intense resonance at $g_{\text{eff}} = 6.35$ with broader major signals at $g_{\text{eff}} = 2.55$ and 1.57 (Figure 10, middle). These features were simulated as an $S = 3/2$ spin system with the g and D values from the magnetization, also introducing $E/D = 0.333$. Similar to the spectrum of **8**, D strain of 5 cm^{-1} (17% of D) was necessary to account for line shapes. Unresolved hyperfine coupling to the ammine ^{14}N nucleus may also contribute to broadening. There are small signals at $g = 4.4$ and 2 that may come from the unknown decomposition product discussed in the synthesis section.

The magnetization curves for ammonia complex **10** show a pronounced field dependence with saturation occurring around $2.7 \mu_B$. They were fit to $g = [2.01, 2.01, 2.07]$ ($g_{\text{iso}} = 2.03$) and $D = -3.5(1) \text{ cm}^{-1}$ (Figure S66, bottom). Fitting with $D = +3.5 \text{ cm}^{-1}$ also gave acceptable agreement with experimental data. At 10 K, the EPR spectrum of **10** shows features at $g_{\text{eff}} = 6.15, 4.75$, and 3.40, while signals at 2.36, 2.07, 2.05, and 1.99 are assigned to impurities (Figure 10, bottom). The spectrum was simulated as $S = 3/2$ with $E/D = 0.106$ using the g and negative D from the magnetization fit. An $S = 1/2$ impurity with $g = [2.07, 2.05, 1.99]$ was included in the simulation in 1% relative abundance to the major $S = 3/2$ signal. D strain of 2.4 cm^{-1} (57% of D) was applied to account for the broad line shapes, though like **9**, broadening could be compounded by unresolved hyperfine coupling to the ammine ^{14}N nucleus. A spectrum similar to that of **10** was

reported for a square pyramidal ferric intermediate spin complex with $E/D = 0.107$.⁶⁶ Simulations of the EPR spectrum with $D = +3.5 \text{ cm}^{-1}$ had a much smaller $g = 6.15$ component, which is inconsistent with the relatively intense signal seen experimentally. The $g = 6.15$ signal is most likely associated with transitions within the $|\pm 3/2\rangle$ doublet, and its high intensity at 10 K suggests that the ground state is $|\pm 3/2\rangle$, i.e. $D < 0$.

The magnetization and EPR fit parameters are summarized in Table 2. Our magnetization data suggests that $D < 0$ for **8** and **9**, and the intense absorption at $g = 6.15$ in the spectrum of **10** suggests the sign of D is negative in this compound as well.

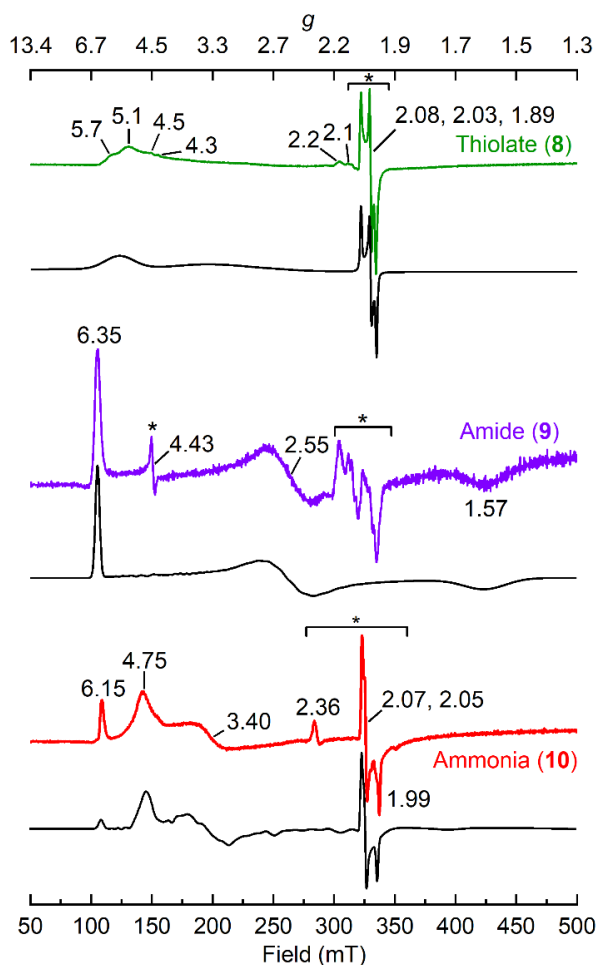


Figure 10. X-band (frequency = 9.37 GHz) EPR spectra from 50 to 500 mT of thiolate complex **8** (top, green) at ~10 K, amide complex **9** (middle, purple) at ~5 K, and ammonia complex **10** (bottom, red) at ~10 K as 1 mM solutions in MeTHF. Each spectrum was collected using a 19 G modulation amplitude and a microwave power of either 0.064 mW (**8**) or 0.020 mW (**9** and **10**). Fits are plotted as black traces beneath their respective experimental spectrum. Signals marked by asterisks are assigned to impurities, which were modeled as $S = 1/2$ species for **8** and **10** in 1% relative concentration to the $S = 3/2$ species.

Table 2. Key parameters for the simulations of the EPR spectra and magnetization data of complexes **8-10**.

	g_x, g_y, g_z	g_{iso}	D	E/D
8	2.30, 2.30, 1.89	2.16	− 28(1)	0.200
9	2.15, 2.54, 2.33	2.34	− 30(2)	0.333
10	2.01, 2.01, 2.07	2.03	− 3.5(1)	0.106

Mössbauer Spectroscopy of S and N Donor Complexes. Zero-field Mössbauer spectra of solid thiolate complexes **8** and **8-crown**, N(TMS)₂ amide complexes **9** and **9-crown**, and ammonia complex **10** were recorded at 80 K. The spectra of **8**, **9**, and **10** are shown in Figure 11, and fit parameters in Table 3. The isomer shifts and large quadrupole splitting values of **8**, **8-crown**, and **10** are within the expected ranges for intermediate spin iron(III), and are broadened with Γ of 0.5 to 0.6 mm/s.⁶³ The spectrum of **9**, however, shows an isomer shift of only 0.18 mm/s, a markedly low quadrupole splitting of 0.93 mm/s, and narrower lines with $\Gamma = 0.3$ mm/s. The Mössbauer parameters of **8-crown** ($\delta = 0.30$ mm/s, $|\Delta E_Q| = 4.03$ mm/s) and **9-crown** ($\delta = 0.17$ mm/s, $|\Delta E_Q| = 0.88$ mm/s) are nearly the same as their crown-free versions **8** and **9**.

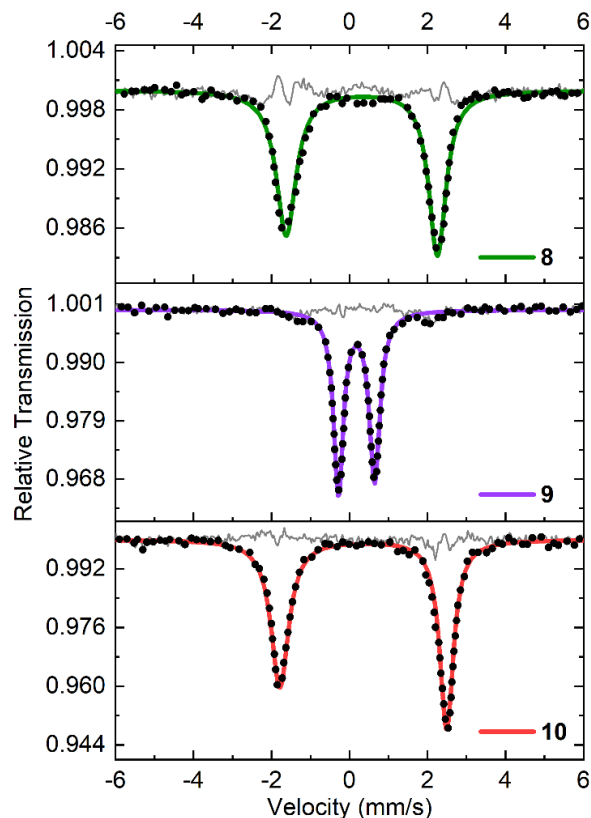


Figure 11. Zero field Mössbauer spectra of solid **8**, **9**, and **10** at 80 K. Data are plotted as black circles and residual as gray trace. **8**: $\delta = 0.31$ mm/s, $|\Delta E_Q| = 3.88$ mm/s, $\Gamma_L = 0.61$ mm/s, $\Gamma_R = 0.54$ mm/s. **9**: $\delta = 0.18$ mm/s, $|\Delta E_Q| = 0.93$ mm/s, $\Gamma_L = 0.31$ mm/s, $\Gamma_R = 0.33$ mm/s; there is a 4% impurity with parameters matching **5-Et₂O**. **10**: $\delta = 0.35$ mm/s, $|\Delta E_Q| = 4.28$ mm/s, $\Gamma_L = 0.55$ mm/s, $\Gamma_R = 0.43$ mm/s.

In order to understand this difference, we used the ORCA quantum chemistry program in conjunction with a published isomer shift correlation to calculate the Mössbauer parameters of **8**, **9**, and **10** using DFT at the B3LYP/ZORA-def2-TZVP level of theory.⁶⁷ All initial Mössbauer computations were carried out on BP86-optimized structures from X-ray diffraction data in the

quartet spin state in accordance with experimental evidence. No counterions were included for anionic **9** and **10**, as previous studies have indicated that Mössbauer predictions are largely independent of the counterion.⁶⁸⁻⁶⁹ These potassium-free calculated parameters were in agreement with the experimental Mössbauer parameters of thiolate complex **8** and ammonia complex **10**, but both δ and $|\Delta E_Q|$ of amide complex **9** were overestimated by 0.11 mm/s and 3.18 mm/s, respectively (Table 3).

Table 3. Comparison between the experimental and calculated Mössbauer parameters for anionic **8**, anionic **9**, and neutral **10**. The sign of the experimental quadrupole splitting is undetermined.

Complex	δ (mm/s)		ΔE_Q (mm/s)	
	Exp.	Calc'd	Exp.	Calc'd
8	0.31	0.28	3.88	+ 3.97
9	0.18	0.29	0.93	− 4.24
10	0.35	0.33	4.28	+ 4.34

Since the crystal structure of **9** shows a potassium cation only 3.13 Å from one S atom in the SCS pincer, we hypothesized that including K⁺ may be necessary to properly describe its electronic structure. Thus, we started from the crystallographic structure of **9** and performed Mössbauer calculations on structures that included K⁺: one with geometry optimization of all atoms (model A) and one with only H atoms optimized (model B) (Figure 12). Model C in Figure 12 is the optimized structure of potassium-free **9**, whose predicted Mössbauer parameters are listed in Table 3. In the crystal structure, the potassium is also coordinated to a Dipp aryl group of a neighboring molecule of **9**, and this second arene was modeled as benzene in the calculations.

Mössbauer calculations on models A and B predicted parameters in agreement with experiment for **9** despite a significant distortion of the pincer plane in model A (Figure 12). Model

A is predicted to have $\delta = 0.19$ mm/s and $\Delta E_Q = 0.97$ mm/s while B is predicted to have $\delta = 0.22$ mm/s and $\Delta E_Q = 0.84$ mm/s. The Mössbauer calculations on model C give a very different quadrupole splitting, and these are listed in Table 3 as the calculated parameters of **9**. These results are summarized in Figure 12, and the drastic difference will be discussed below.

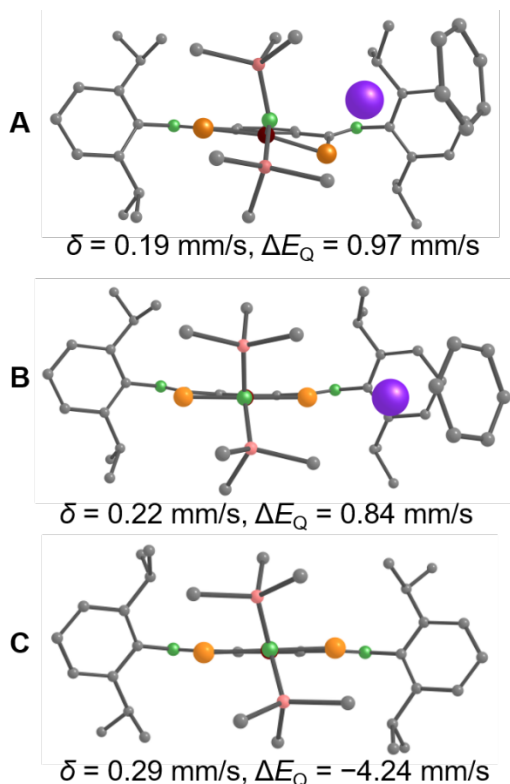


Figure 12. Structures viewed along the N-Fe-C bonds of three models of **9** after BP86/ZORA-def2-TZVP optimization, with their predicted Mössbauer parameters stated below. Model **A**: all-atom optimization in presence of K^+ . Model **B**: H-atom optimization in presence of K^+ . Model **C**: all-atom optimization without K^+ . Potassium is represented as a purple sphere.

Analogously, we performed Mössbauer calculations on all-atom-optimized **9-crown** with potassium included. This structure gave $\delta = 0.16$ mm/s and $\Delta E_Q = -0.91$ mm/s, in agreement with

experimental values for **9-crown** despite the potassium being formally outer sphere with an Fe...K distance of 8.026 Å. The Löwdin charge on potassium was found to be -0.06 in this structure, suggesting significant delocalization of positive charge onto the coordinated THF and crown ether components. To test the isolated effect of a distant and free potassium ion, we removed the two THF molecules and the 18-crown-6 that were coordinated to potassium in optimized **9-crown** and repeated the Mössbauer calculations (Figure S95). This model gave $\delta = 0.33$ mm/s and $\Delta E_Q = -4.08$ mm/s, which is not close to the experimental spectrum of **9-crown** and instead is much closer to that calculated for model C (anionic **9**). In contrast to the structure containing THF and 18-crown-6, the Löwdin charge on potassium was found to be +0.99 in this structure. These results indicate that the THF and 18-crown-6 may be accepting most of the positive charge of the potassium cation, which then places enough positive charge close to the iron to alter its electronic structure. Charge reorganization, albeit in varying degrees, has been implicated as a stabilizing factor in the formation of alkali-crown complexes in previous theoretical studies.⁷⁰⁻⁷¹ Additionally, although the anionic model of thiolate complex **8** was in agreement with experiment, we calculated Mössbauer parameters for optimized **8-crown** with potassium included to evaluate its consistency with experiment. This calculation gave $\delta = 0.28$ mm/s and $\Delta E_Q = 3.96$ mm/s, also in agreement with the spectrum of **8-crown** and essentially unchanged from the potassium-free predictions for **8** that are shown in Table 3. Taken together, the experimental and computed Mössbauer spectra for the models described above suggest that the amide donor in **9** leads to an unusual situation in which its electronic structure is dependent on the presence of a nearby cation.

To compare the electronic structures of the computational models whose Mössbauer parameters match experiment to those that do not, we plotted the frontier quasi-restricted orbitals (QROs) for models A (reproduces experimental Mössbauer parameters; all atoms optimized with

K⁺) and C (does not reproduce experimental Mössbauer parameters; all atoms optimized without K⁺) in Figure 13. The QROs show that the shape of the doubly-occupied d orbital (DOMO) for model A resembles d_{z^2} while the doubly-occupied d orbital for model C resembles d_{yz} . The d_{z^2} DOMO has 3.7% Fe s character, while the d_{yz} DOMO has 0.0% Fe s character, explaining the significant change in the isomer shift. The ordering of the d_{xz} and d_{xy} orbitals is also switched, but the $d_{x^2-y^2}$ orbital is always higher in energy than the remaining four d orbitals due to its σ antibonding interactions with the SCS pincer. QRO analysis of optimized **9-crown** shows the same d orbital ordering as model A (all atoms optimized with K⁺), though d_{z^2} is 0.90 eV more stabilized than d_{xy} in **9-crown**. (Figure S96)

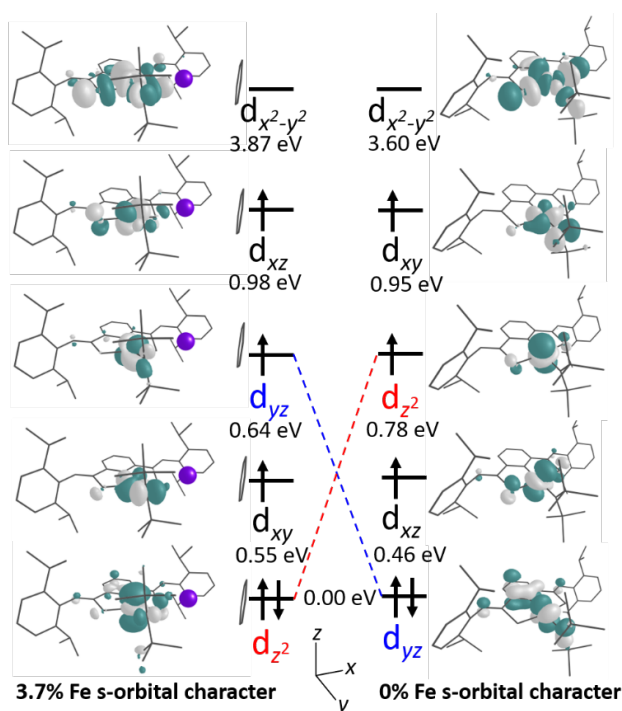


Figure 13. QRO plots at an isovalue of 0.03 au of the d-assigned orbitals for amide complex **9** from model A (left, all atoms optimized with K⁺) and model C (right, all atoms optimized without K⁺). Energies relative to the doubly-occupied orbital are listed below the d orbital assignment. The

structure of the iron complex is shown in gray wireframe, and potassium is represented as a purple sphere.

Additional experiments were performed to probe the influence of the cation on the electronic structure of **9**. First, we computationally sampled a wide range of potential locations for a positive charge to learn about the orientational dependence, but the results were not conclusive (Figure S97). In addition, we experimentally sought to “remove” the potassium completely by reacting starting material **5-Et₂O** with N(TMS)₂ in the presence of excess (two equiv) of [2.2.2]cryptand per N(TMS)₂ group (Scheme S1). The reaction conditions were otherwise identical to the syntheses of **9** and **9-crown**. The Mössbauer spectrum of the dried crude reaction mixtures showed a mixture of two components: one with parameters close to **9** ($\delta = 0.17$ mm/s, $|\Delta E_Q| = 0.82$ mm/s) and one with $\delta = 0.37$ mm/s and $|\Delta E_Q| = 3.27$ mm/s (Figure S92). The parameters of the component with a larger isomer shift and quadrupole splitting than **9** do not correspond to any other compound in this work. Though we were unable to identify or obtain full conversion to the component with large δ and $|\Delta E_Q|$, this new Mössbauer signal has parameters that are more similar to those predicted for anionic **9**, which represents the extreme in which iron and K⁺ are too far apart to interact.

DISCUSSION

Relationship between Protonation State and Reduction Potential. To our knowledge, bond dissociation free energies of thioamide SCS pincer compounds have not been reported prior to this work. The N–H BDFE of **2** (56 kcal/mol) is substantially lower than the computed BDEs for free thioamides (90–100 kcal/mol), and its pK_a of ~21 indicates that the N–H proton is many

orders of magnitude less acidic than free thioamides, which lie in the range 11–15 (Figure 14).⁷²⁻
⁷⁴ It is seen from the Bordwell equation that the high pK_a of **2** raises the BDFE relative to organic thioamides, but the very negative reduction potential ($E_{1/2} = -1.42$ V vs. Fc^+/Fc) of the iron(II) center lowers the BDFE to a much larger extent. This potential is 1.0 V more negative than $E_{1/2}$ for the $\text{Fe}^{3+/2+}$ couple in a four-coordinate SNS pincer complex with an NHC as the fourth ligand, and 1.4 V more negative than the analogous five-coordinate SNS scaffold with two THF molecules.⁴¹ The more negative reduction potential in our system may result from the negatively-charged aryl pincer in place of the pyridine pincer, and also from the coordination of three strong phosphine donors.

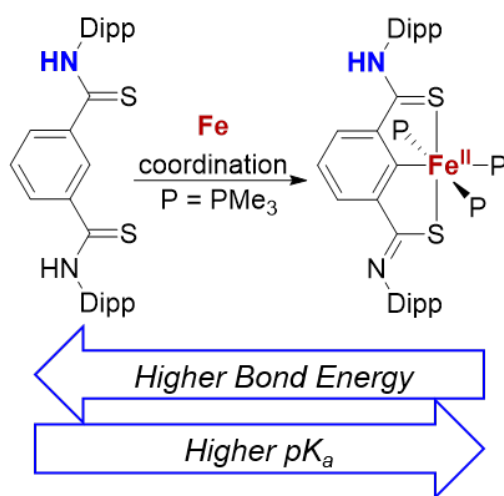


Figure 14. Summary of the effect of iron coordination on the bond energy and pK_a of the thioamide N–H site.

Although the N–H BDFE of **3** is significantly lower than those of free thioamides, it is comparable to other iron systems with N–H bonds in the supporting ligand. In a recent example, the N–H BDFEs of aminobenzenethiolate iron(II) complexes supported by a TACN ligand were

determined by measurement of pK_a and $E_{1/2}$.⁷⁵ In the parent system, the $Fe^{3+/2+}$ redox couple was found at $E_{1/2} = -0.84$ V, and the pK_a was determined to be ≥ 19.5 , giving a BDFE of ≥ 62 kcal/mol; bracketing showed an exact BDFE near 68 kcal/mol. Studies of nickel, platinum, and ruthenium SCS compounds also corroborate decreased N–H bond acidity and more negative reduction potential upon metalation, though these examples do not report bond energies.^{39, 76-78}

There are interesting implications of our determination that deprotonating a distant thioamide site gives a highly-reducing iron(II) species, because this could be a mechanism for generating electron-rich active sites in metalloenzymes. This fits into a growing body of evidence that reduction potentials can may be modulated by the protonation state of sites outside the vicinity of metals in metallocofactors like the nitrogenase FeMoco.^{51, 79}

Electronic Structure. The EPR spectrum of **9** is notable for its high rhombicity. While the spectrum resembles a few other $S = 3/2$ examples of well-defined iron complexes with large E/D ,⁸⁰⁻⁸¹ the most notable comparison is to a square planar $S = 3/2$ cobalt(II) ONO pincer complex with a chloride fourth donor.⁸² Structurally, this dianionic complex is reminiscent of **9**, with the ONO pincer coordinating through a central amido N donor and lithium counterions flanking the alkoxide arms of the pincer ligand. The EPR spectrum of this complex was also highly rhombic, with $E/D \geq 0.25$, maximum g_{eff} of 7.35, and $g_y > g_x, g_z$. DFT calculated d orbital energies revealed an unusual doubly-occupied d_z^2 orbital, and the EPR spectrum was rationalized on the basis of strong spin-orbit coupling of the ground state with the $d_z^2(\beta) \rightarrow d_{yz}$ and $d_{xy}(\beta) \rightarrow d_{xz}$ excited states. In our case, mixing of the ground state with an excited state created by promotion of $d_z^2(\beta)$ into the half-filled d_{yz} orbital could also account for the large deviation in g from g_e in **9**.

Sulfur, nitrogen, or mixed sulfur/nitrogen donors like in **8-11** are found in several other non-porphyrin ferric intermediate spin complexes.^{80, 83-88} These examples all also have near square

planar or square pyramidal geometries. Mössbauer spectra of ferric $S = 3/2$ complexes generally have isomer shifts around 0.3 mm/s and large quadrupole splitting.⁶³ Though Mössbauer spectra of complexes **8** (thiolate) and **10** (ammine) show normal δ and $|\Delta E_Q|$ for this class of compounds, the spectrum of **9** (amide) is an outlier in line width, isomer shift, and quadrupole splitting. In regard to line widths, the 80 K spectra of both **8** and **10** consist of broadened asymmetric doublets. Broad, asymmetric doublets at 80 K in intermediate-spin iron(III) complexes are a marker of slow magnetic relaxation in the range of 10^{-8} s to 10^{-11} s; i.e., faster than the nuclear excited state lifetime of ^{57}Fe ($\sim 10^{-8}$ s) but slower than the $\sim 10^{-12}$ s that would give negligible paramagnetic broadening.^{63, 87, 89} The smaller line widths of **9** relative to those in **8** and **10** indicate that paramagnetic relaxation is faster, which is attributable to its larger E/D that mixes the Kramers doublets.⁹⁰⁻⁹¹ To our knowledge, the quadrupole splitting values of **9** and **9-crown** are the lowest reported for any intermediate-spin iron(III) complex, though anomalously small quadrupole splitting has also been reported in a few $S = 2$ iron(II) complexes with planar ligand environments.⁹²⁻⁹³ Planar ligand scaffolds can induce large positive contributions to the electric field gradient (EFG) on the axis perpendicular to the ligand plane (usually assigned as the z axis), and the Mössbauer quadrupole splitting is proportional to the z -component of the EFG.^{63, 92} Interestingly, computational analysis of the cited systems with anomalously small ΔE_Q also revealed a doubly-occupied d_{z^2} orbital, as we found for **9** (Figure 13). Thus, the small ΔE_Q values imply that the large positive contribution to the z -component of the electric field gradient by the planar ligand is counteracted by a large negative contribution from the d_{z^2} ground state. Double occupation of the d_{z^2} orbital also accounts for the decreased isomer shift (which decreases with increasing iron s -electron density) of **9** by greater mixing of the doubly-occupied $3d_{z^2}$ with the $4s$ orbital,⁹⁴ which is corroborated by our DFT calculations.

The question that arises is then: why do amide complexes **9** and **9-crown** show evidence for a d_z^2 ground state electronic structure while thiolate complexes **8** and **8-crown** as well as ammonia complex **10** do not? First, we propose that the π -donating orbitals of the $N(TMS)_2$ ligand in **9** exert a stronger destabilizing influence on the π -symmetry iron d_{xy} and d_{yz} orbitals than the thiolate donor in **8** and certainly more than the ammine donor in **10**. Our proposition of a stronger interaction in **9** than **8** is tied to its structure, which shows a short Fe–N bond and a nearly 90° angle between the $N(TMS)_2$ plane and the pincer plane, permitting excellent overlap between d_{xy} and the N p_x orbital and the d_{yz} and sp^2 -like orbitals aligned roughly along the N–Si bonds. This highly π -donating ligand field closes the energy gap between d_z^2 and d_{xz}/d_{yz} in the typical square planar splitting pattern. This explanation alone does not account, however, for the extreme variability in the calculated Mössbauer parameters for **9** depending on whether there is a positive charge near iron. On the basis of our DFT results, we therefore also suggest that the d_z^2 orbital can be further stabilized by the presence of a nearby positive charge. Though the complete description of the cation interaction with each of the d orbitals is not elucidated by our work, selective stabilization of the d_z^2 orbital may be a result of its shape. A positive charge in the plane of the pincer could interact with the torus-shaped portion of the d_z^2 orbital, and one along the z axis can interact with the lobes pointing above and below the pincer plane. The stabilizing interaction of charge with the lobes of d_z^2 is illustrated by the comparison between the QRO energies of model A in Figure 13 with optimized **9-crown** (Figure S96). Model A has positive charge with non-zero projections both onto the z axis and xy -plane while **9-crown** has positive charge that is along the z axis. Accordingly, the d_z^2 orbital is 0.35 eV lower in energy than the DOMO+1 in **9-crown** versus model A.

The influence of the alkali metal cation is a distinctive aspect of the work reported here, and it pushes forward the growing understanding of the potential tuning role of cations near a transition-metal center. In a relevant example, Yang has shown that appended cations cause substantial electric fields,⁹⁵ which can have beneficial influences on catalysis.⁹⁶⁻⁹⁷ Electronic structure calculations in these systems did not show that the orbital energies were differentially affected by the cation, leading to the conclusion that the cation mainly exerts an electrostatic effect. Tolman has shown the influences of nearby cations on O–H bond dissociation energies.⁹⁸ In more recent work, Tomson observed shifts in redox potentials that were attributed to stabilization of a d_{z^2} orbital, and supported this idea with DFT calculations.⁹⁹ Redox potentials were primarily used to probe cation effects in these examples, but incorporation of iron in our complexes enabled us to use Mössbauer spectra that can be directly related to the electronic structure of iron. Through the combination of spectroscopy and DFT, we identified cation-dependent changes in orbital energetics. While the overall spin state is conserved throughout, a β electron shifts to a cation-stabilized d_{z^2} orbital, manifested in Mössbauer spectra by low δ and $|\Delta E_Q|$. In the future, this effect may be utilized to control reactivity that depends on the ordering of orbital energies.

The conclusions from our electronic structure studies of complexes **8** (thiolate), **9** (amide), and **10** (ammine) utilizing EPR spectroscopy, SQUID magnetometry, Mössbauer spectroscopy, and DFT calculations are summarized as follows. EPR spectroscopy in combination with variable-temperature measurements demonstrated large negative D with $E \neq 0$ in each case. Mössbauer spectra of **8** and **10** showed isomer shifts and quadrupole splitting values consistent with other known intermediate spin iron(III) complexes, and DFT could accurately predict these parameters without including a counterion in **8**. The quadrupole splitting of **9**, however, was anomalously low, and DFT predicted a large $|\Delta E_Q|$ when no counterion was included. Inclusion of potassium in the

model of **9** gave calculated Mössbauer parameters in agreement with experiment, and the energetic ordering of d_{z^2} relative to the other d orbitals is likely to determine whether a typical large $|\Delta E_Q|$ versus an atypical small $|\Delta E_Q|$ is observed. *Independently*, the relatively low distortion from planarity, strong π donation from the amide ligand, and short Fe–N bond in **9** are hypothesized to enact relative orbital energies that are amenable to changing order in the presence of a cation. Clearly, the SCS scaffold gives access to a range of electronic structures depending on the identity of the fourth donor ligand and on the cation location.

Comparisons to the Nitrogenase FeMoco. The C and S-ligated iron complexes have the same donor atoms as the iron sites in the FeMoco, and we briefly explore the comparison of molecular and electronic structures. The most thoroughly-characterized state of FeMoco is the enzyme resting state (E_0), and in this structure, the high-spin belt irons are bridged by sulfide ligands and share a central carbide, leading to a 3S/1C environment.¹² Our complex **8** likewise has an iron center ligated exclusively by three S donors and one C donor. Its Fe–C bond length of 2.00 Å is very close to the 2.01 Å Fe–C distance in FeMoco.^{13-14, 100} The Fe–S lengths, which range from 2.24 to 2.25 Å, are also highly similar to Fe–S bond lengths in FeMoco (2.25 to 2.27 Å). Despite being in an intermediate spin state, these bond distances are closer to those in resting state FeMoco than the two previously-reported (SCS)iron complexes, which were in lower oxidation states and thus had longer Fe–C/S bonds.^{26, 28}

The final state of the enzyme during catalysis is an iron-ammonia adduct (E_8).¹⁰¹ Because turnover from E_8 to E_0 is redox neutral, ammonia would be expected to bind to either the iron(II) or iron(III) oxidation states.¹⁰¹ We were able to isolate the stable ammonia adduct in high yield in an intermediate-spin iron(III) oxidation state, thus demonstrating the feasibility of an iron(III) ammonia adduct in a C and S-ligand field.

CONCLUSIONS

A new pincer ligand bearing only sulfur and carbon donor atoms can support new iron complexes. The ligand scaffold has a proton-responsive site, gives access to unusual electron structures, and mimics the sulfide and carbide donors found in the cofactor of nitrogenase enzymes. Adducts of thiolate, amide, ammonia, and CO demonstrate the versatility of this SCS pincer system to support a variety of nitrogenase-relevant donors that induce an electronic structure that is highly sensitive to the iron surroundings.

ACKNOWLEDGMENTS

We gratefully acknowledge funding from the National Institutes of Health (R01-GM065313 to P.L.H.; F32-GM126656 to K.L.S.; R35-GM124908 to K.M.L.). We thank Majed Fataftah for assistance with magnetism interpretation. We thank Nicholas Bingham for collecting SQUID magnetometry measurements. We thank the Yale Center for Research Computing for guidance and use of the research computing infrastructure, specifically Thomas Langford. We thank Jessica Freeze for assistance with computer scripting. XAS data were obtained at the Stanford Synchrotron Radiation Lightsource, SLAC National Accelerator Laboratory, which is supported by the U.S. Department of Energy, Office of Science, Office of Basic Energy Sciences under Contract No. DE-AC02-76SF00515. The SSRL Structural Molecular Biology Program is supported by the DOE Office of Biological and Environmental Research, and by the National Institutes of Health, National Institute of General Medical Sciences (P30GM133894).

REFERENCES

1. Bolm, C.; Legros, J.; Le Pailh, J.; Zani, L. Iron-Catalyzed Reactions in Organic Synthesis. *Chem. Rev.* **2004**, *104*, 6217-6254.
2. Walker, F. A.; Simonis, U., Iron Porphyrin Chemistry. In *Encyclopedia of Inorganic Chemistry*, John Wiley & Sons: New York, 2006.
3. Bauer, I.; Knölker, H.-J. Iron Catalysis in Organic Synthesis. *Chem. Rev.* **2015**, *115*, 3170.
4. Fürstner, A. Iron Catalysis in Organic Synthesis: A Critical Assessment of What It Takes To Make This Base Metal a Multitasking Champion. *ACS Cent. Sci.* **2016**, *2*, 778-789.
5. Shang, R.; Ilies, L.; Nakamura, E. Iron-Catalyzed C–H Bond Activation. *Chem. Rev.* **2017**, *117*, 9086-9139.
6. Wei, D.; Darcel, C. Iron Catalysis in Reduction and Hydrometalation Reactions. *Chem. Rev.* **2019**, *119*, 2550-2610.
7. Tard, C.; Pickett, C. J. Structural and Functional Analogues of the Active Sites of the [Fe]-, [NiFe]-, and [FeFe]-Hydrogenases. *Chem. Rev.* **2009**, *109*, 2245-2274.
8. Bart, S. C.; Chłopek, K.; Bill, E.; Bouwkamp, M. W.; Lobkovsky, E.; Neese, F.; Wieghardt, K.; Chirik, P. J. Electronic Structure of Bis(imino)pyridine Iron Dichloride, Monochloride, and Neutral Ligand Complexes: A Combined Structural, Spectroscopic, and Computational Study. *J. Am. Chem. Soc.* **2006**, *128*, 13901-13912.
9. Volbeda, J.; Meetsma, A.; Bouwkamp, M. W. Electron-Deficient Iron Alkyl Complexes Supported by Diimine Ligand (Ph₂CN)₂C₂H₄: Evidence for Reversible Ethylene Binding. *Organometallics* **2009**, *28*, 209-215.
10. Holland, P. L. Distinctive Reaction Pathways at Base Metals in High-Spin Organometallic Catalysts. *Acc. Chem. Res.* **2015**, *48*, 1696-1702.

11. Sears, J. D.; Neate, P. G. N.; Neidig, M. L. Intermediates and Mechanism in Iron-Catalyzed Cross-Coupling. *J. Am. Chem. Soc.* **2018**, *140*, 11872-11883.
12. Lancaster, K. M.; Römel, M.; Ettenhuber, P.; Hu, Y.; Ribbe, M. W.; Neese, F.; Bergmann, U.; DeBeer, S. X-ray Emission Spectroscopy Evidences a Central Carbon in the Nitrogenase Iron-Molybdenum Cofactor. *Science* **2011**, *334*, 974-977.
13. Spatzal, T.; Aksoyoglu, M.; Zhang, L.; Andrade, S. L. A.; Schleicher, E.; Weber, S.; Rees, D. C.; Einsle, O. Evidence for Interstitial Carbon in Nitrogenase FeMo Cofactor. *Science* **2011**, *334*, 940-940.
14. Einsle, O.; Rees, D. C. Structural Enzymology of Nitrogenase Enzymes. *Chem. Rev.* **2020**, *120*, 4969-5004.
15. Poli, R. Open-Shell Organometallics as a Bridge between Werner-Type and Low-Valent Organometallic Complexes. The Effect of the Spin State on the Stability, Reactivity, and Structure. *Chem. Rev.* **1996**, *96*, 2135-2204.
16. Schröder, D.; Shaik, S.; Schwarz, H. Two-State Reactivity as a New Concept in Organometallic Chemistry. *Acc. Chem. Res.* **2000**, *33*, 139-145.
17. Shaik, S.; Hirao, H.; Kumar, D. Reactivity of High-Valent Iron–Oxo Species in Enzymes and Synthetic Reagents: A Tale of Many States. *Acc. Chem. Res.* **2007**, *40*, 532-542.
18. Lutz, S. A.; Hickey, A. K.; Gao, Y.; Chen, C.-H.; Smith, J. M. Two-State Reactivity in Iron-Catalyzed Alkene Isomerization Confers σ -Base Resistance. *J. Am. Chem. Soc.* **2020**, *142*, 15527-15535.
19. Čorić, I.; Holland, P. L. Insight into the Iron–Molybdenum Cofactor of Nitrogenase from Synthetic Iron Complexes with Sulfur, Carbon, and Hydride Ligands. *J. Am. Chem. Soc.* **2016**, *138*, 7200-7211.
20. Speelman, A. L.; Holland, P. L., Sulfur-Supported Iron Complexes for Understanding N₂ Reduction. In *Nitrogen Fixation*, Nishibayashi, Y., Ed. Springer International Publishing: Cham, 2017; pp 197-213.
21. Tanifuji, K.; Ohki, Y. Metal–Sulfur Compounds in N₂ Reduction and Nitrogenase-Related Chemistry. *Chem. Rev.* **2020**, *120*, 5194-5251.

22. Imamura, Y.; Kubo, K.; Mizuta, T.; Miyoshi, K. Reactions of Ring-Slipped Iron Complexes Derived from P(S)Ph-Bridged [1]Ferrocenophane: Synthesis of Bis(half-sandwich) Heterodinuclear Complexes. *Organometallics* **2006**, *25*, 2301-2307.
23. Chen, Y.; Zhou, Y.; Chen, P.; Tao, Y.; Li, Y.; Qu, J. Nitrogenase Model Complexes: Synthesis, Structure, and Catalytic N-N Bond Cleavage of Hydrazines on Diiron Centers. *J. Am. Chem. Soc.* **2008**, *130*, 15250-15251.
24. Chen, Y.; Liu, L.; Peng, Y.; Chen, P.; Luo, Y.; Qu, J. Unusual Thiolate-Bridged Diiron Clusters Bearing the cis-HN=NH Ligand and Their Reactivities with Terminal Alkynes. *J. Am. Chem. Soc.* **2011**, *133*, 1147-1149.
25. Li, Y.; Li, Y.; Wang, B.; Luo, Y.; Yang, D.; Tong, P.; Zhao, J.; Luo, L.; Zhou, Y.; Chen, S.; Cheng, F.; Qu, J. Ammonia formation by a thiolate-bridged diiron amide complex as a nitrogenase mimic. *Nat. Chem.* **2013**, *5*, 320-326.
26. Čorić, I.; Mercado, B. Q.; Bill, E.; Vinyard, D. J.; Holland, P. L. Binding of dinitrogen to an iron-sulfur-carbon site. *Nature* **2015**, *526*, 96-99.
27. Yang, D.; Li, Y.; Wang, B.; Zhao, X.; Su, L.; Chen, S.; Tong, P.; Luo, Y.; Qu, J. Synthesis and Electrocatalytic Property of Diiron Hydride Complexes Derived from a Thiolate-Bridged Diiron Complex. *Inorg Chem* **2015**, *54*, 10243-10249.
28. Speelman, A. L.; Skubi, K. L.; Mercado, B. Q.; Holland, P. L. Synthesis and Reactivity of Iron Complexes with a Biomimetic SCS Pincer Ligand. *Inorg. Chem.* **2021**, *60*, 1965-1974.
29. Sun, T.; Xu, S.; Yang, D.; Su, L.; Wang, B.; Qu, J. Catalytic Disproportionation of Hydrazine Promoted by Biomimetic Diiron Complexes with Benzene-1,2-Dithiolate Bridge Modified by Different Substituents. *Eur. J. Inorg. Chem.* **2020**, *2020*, 4263-4269.
30. Speelman, A. L.; Čorić, I.; Van Stappen, C.; DeBeer, S.; Mercado, B. Q.; Holland, P. L. Nitrogenase-Relevant Reactivity of a Synthetic Iron-Sulfur-Carbon Site. *J. Am. Chem. Soc.* **2019**, *141*, 13148-13157.

31. Rochon, F. D.; Melanson, R.; Andruh, M. The influence of different N-substituted diethylenetriamine ligands on the aggregation of copper(II) monoacetato complexes. *Polyhedron* **1996**, *15*, 3075-3084.
32. Bergbreiter, D. E.; Osburn, P. L.; Liu, Y.-S. Tridentate SCS Palladium(II) Complexes: New, Highly Stable, Recyclable Catalysts for the Heck Reaction. *J. Am. Chem. Soc.* **1999**, *121*, 9531-9538.
33. Manen, H.-Jan v.; Nakashima, K.; Shinkai, S.; Kooijman, H.; Spek, Anthony L.; Veggel, Frank C. J. M. v.; Reinhoudt, David N. Coordination Chemistry of SCS Pd^{II} Pincer Systems. *Eur. J. Inorg. Chem.* **2000**, *2000*, 2533-2540.
34. Begum, R. A.; Powell, D.; Bowman-James, K. Thioamide Pincer Ligands with Charge Versatility. *Inorg Chem* **2006**, *45*, 964-966.
35. Mehendale, N. C.; Lutz, M.; Spek, A. L.; Klein Gebbink, R. J. M.; van Koten, G. Self-assembly of para-OH functionalized ECE-metalated pincer complexes. *J. Organomet. Chem.* **2008**, *693*, 2971-2981.
36. Kruithof, C. A.; Berger, A.; Dijkstra, H. P.; Soulimani, F.; Visser, T.; Lutz, M.; Spek, A. L.; Gebbink, R. J. M. K.; van Koten, G. Sulfato-bridged ECE-pincer palladium(II) complexes: structures in the solid-state and in solution, and catalytic properties. *Dalton Trans.* **2009**, 3306-3314.
37. Okamoto, K.; Kanbara, T.; Yamamoto, T.; Wada, A. Preparation and Characterization of Luminescent SCS and NCN Pincer Platinum Complexes Derived from 3,5-Bis(anilinothiocarbonyl)toluene. *Organometallics* **2006**, *25*, 4026-4029.
38. Kuwabara, J.; Kanbara, T. Synthesis and Optical Properties of Pincer Palladium and Platinum Complexes having Thioamide Units. *J. Photopolym. Sci. Technol.* **2008**, *21*, 349-353.
39. Komiyama, Y.; Kuwabara, J.; Kanbara, T. Deprotonation-Induced Structural Changes in SNS-Pincer Ruthenium Complexes with Secondary Thioamide Groups. *Organometallics* **2014**, *33*, 885-891.
40. Suzuki, T.; Kajita, Y.; Masuda, H. Deprotonation/protonation-driven change of the σ -donor ability of a sulfur atom in iron(II) complexes with a thioamide SNS pincer type ligand. *Dalton Trans.* **2014**, *43*, 9732-9739.

41. Suzuki, T.; Matsumoto, J.; Kajita, Y.; Inomata, T.; Ozawa, T.; Masuda, H. Nitrosyl and carbene iron complexes bearing a κ^3 -SNS thioamide pincer type ligand. *Dalton Trans.* **2015**, *44*, 1017-1022.
42. Okamoto, K.; Kuwabara, J.; Kanbara, T. Secondary Thioamides as Multidentate Ligands for Functional Metal Complexes. *Chem. Lett.* **2014**, *44*, 102-110.
43. Lee, C. M.; Kumler, W. D. The Dipole Moment and Structure of Thiolactams. *J. Org. Chem.* **1962**, *27*, 2052-2054.
44. Hoffman, B. M.; Lukoyanov, D.; Yang, Z.-Y.; Dean, D. R.; Seefeldt, L. C. Mechanism of Nitrogen Fixation by Nitrogenase: The Next Stage. *Chem. Rev.* **2014**, *114*, 4041-4062.
45. Raugei, S.; Seefeldt, L. C.; Hoffman, B. M. Critical computational analysis illuminates the reductive-elimination mechanism that activates nitrogenase for N₂ reduction. *Proc. Natl. Acad. Sci. U.S.A.* **2018**, *115*, E10521.
46. Dance, I. The controlled relay of multiple protons required at the active site of nitrogenase. *Dalton Trans.* **2012**, *41*, 7647-7659.
47. McKee, M. L. A New Nitrogenase Mechanism Using a CFe₈S₉ Model: Does H₂ Elimination Activate the Complex to N₂ Addition to the Central Carbon Atom? *J. Phys. Chem. A* **2016**, *120*, 754-764.
48. Rao, L.; Xu, X.; Adamo, C. Theoretical Investigation on the Role of the Central Carbon Atom and Close Protein Environment on the Nitrogen Reduction in Mo Nitrogenase. *ACS Catal.* **2016**, *6*, 1567-1577.
49. Thorhallsson, A. T.; Benediktsson, B.; Bjornsson, R. A model for dinitrogen binding in the E4 state of nitrogenase. *Chem. Sci.* **2019**, *10*, 11110-11124.
50. Siegbahn, P. E. M. Model Calculations Suggest that the Central Carbon in the FeMo-Cofactor of Nitrogenase Becomes Protonated in the Process of Nitrogen Fixation. *J. Am. Chem. Soc.* **2016**, *138*, 10485-10495.
51. Lampret, O.; Duan, J.; Hofmann, E.; Winkler, M.; Armstrong, F. A.; Happe, T. The roles of long-range proton-coupled electron transfer in the directionality and efficiency of [FeFe]-hydrogenases. *Proc. Natl. Acad. Sci. U.S.A.* **2020**, *117*, 20520.

52. Tyburski, R.; Liu, T.; Glover, S. D.; Hammarström, L. Proton-Coupled Electron Transfer Guidelines, Fair and Square. *J. Am. Chem. Soc.* **2021**, *143*, 560-576.
53. Warren, J. J.; Menzeleev, A. R.; Kretchmer, J. S.; Miller, T. F.; Gray, H. B.; Mayer, J. M. Long-Range Proton-Coupled Electron-Transfer Reactions of Bis(imidazole) Iron Tetraphenylporphyrins Linked to Benzoates. *J. Phys. Chem. Lett.* **2013**, *4*, 519-523.
54. Darcy, J. W.; Koronkiewicz, B.; Parada, G. A.; Mayer, J. M. A Continuum of Proton-Coupled Electron Transfer Reactivity. *Acc. Chem. Res.* **2018**, *51*, 2391-2399.
55. Bisson, A. P.; Hunter, C. A.; Morales, J. C.; Young, K. Cooperative Interactions in a Ternary Mixture. *Chem. Eur. J.* **1998**, *4*, 845-851.
56. Karsch, H. H. Funktionelle Trimethylphosphinderivate, V. Kovalente Methyleisen(II)-Phosphinkomplexe. *Chem. Ber.* **1977**, *110*, 2699-2711.
57. Bhattacharya, P.; Krause, J. A.; Guan, H. Iron Hydride Complexes Bearing Phosphinite-Based Pincer Ligands: Synthesis, Reactivity, and Catalytic Application in Hydrosilylation Reactions. *Organometallics* **2011**, *30*, 4720-4729.
58. Tshepelevitsh, S.; Kütt, A.; Lõkov, M.; Kaljurand, I.; Saame, J.; Heering, A.; Plieger, P. G.; Vianello, R.; Leito, I. On the Basicity of Organic Bases in Different Media. *Eur. J. Org. Chem.* **2019**, *2019*, 6735-6748.
59. Wise, C. F.; Agarwal, R. G.; Mayer, J. M. Determining Proton-Coupled Standard Potentials and X-H Bond Dissociation Free Energies in Nonaqueous Solvents Using Open-Circuit Potential Measurements. *J. Am. Chem. Soc.* **2020**, *142*, 10681-10691.
60. Warren, J. J.; Tronic, T. A.; Mayer, J. M. Thermochemistry of Proton-Coupled Electron Transfer Reagents and its Implications. *Chem. Rev.* **2010**, *110*, 6961-7001.
61. Cao, L.; Jennings, M. C.; Puddephatt, R. J. Amine-Amide Equilibrium in Gold(III) Complexes and a Gold(III)-Gold(I) Auophilic Bond. *Inorg Chem* **2007**, *46*, 1361-1368.
62. Hunt, A. P.; Lehnert, N. The Thiolate Trans Effect in Heme {FeNO}₆ Complexes and Beyond: Insight into the Nature of the Push Effect. *Inorg Chem* **2019**, *58*, 11317-11332.

63. Gütlich, P.; Bill, E.; Trautwein, A. X., *Mössbauer Spectroscopy and Transition Metal Chemistry*. Springer-Verlag: Berlin, Heidelberg, 2011.
64. Sik Min, K.; Weyhermüller, T.; Wieghardt, K. Coordination chemistry of 2-(8-aminoquinolino)-4,6-di-tert-butylphenol with manganese(IV), iron(III), and cobalt(II/III): N,O-coordinated o-iminobenzosemiquinonate(1-) π radical monoanions vs.o-iminophenolate(2-) dianions. *Dalton Trans* **2004**, 178-186.
65. Bittner, M. M.; Lindeman, S. V.; Fiedler, A. T. A Synthetic Model of the Putative Fe(II)-Iminobenzosemiquinonate Intermediate in the Catalytic Cycle of o-Aminophenol Dioxygenases. *J. Am. Chem. Soc.* **2012**, *134*, 5460-5463.
66. De Hont, R. F.; Xue, G.; Hendrich, M. P.; Que, L., Jr.; Bominaar, E. L.; Münck, E. Mössbauer, electron paramagnetic resonance, and density functional theory studies of synthetic $S = 1/2$ Fe(III)-O-Fe(IV)=O complexes. Superexchange-mediated spin transition at the Fe(IV)=O site. *Inorg Chem* **2010**, *49*, 8310-8322.
67. McWilliams, S. F.; Brennan-Wydra, E.; MacLeod, K. C.; Holland, P. L. Density Functional Calculations for Prediction of ^{57}Fe Mössbauer Isomer Shifts and Quadrupole Splittings in β -Diketimate Complexes. *ACS Omega* **2017**, *2*, 2594-2606.
68. Bochevarov, A. D.; Friesner, R. A.; Lippard, S. J. Prediction of ^{57}Fe Mössbauer Parameters by Density Functional Theory: A Benchmark Study. *J. Chem. Theory Comput.* **2010**, *6*, 3735-3749.
69. Zhang, Y.; Oldfield, E. An Investigation of the Unusual ^{57}Fe Mössbauer Quadrupole Splittings and Isomer Shifts in 2 and 3-Coordinate Fe(II) Complexes. *J. Phys. Chem. B* **2003**, *107*, 7180-7188.
70. Glendening, E. D.; Feller, D.; Thompson, M. A. An Ab Initio Investigation of the Structure and Alkali Metal Cation Selectivity of 18-Crown-6. *J. Am. Chem. Soc.* **1994**, *116*, 10657-10669.
71. Hori, K.; Yamada, H.; Yamabe, T. Theoretical study on the nature of the interaction between crown ethers and alkali cations: Relation of interaction energy and ion selectivity. *Tetrahedron* **1983**, *39*, 67-73.
72. Kaur, D.; Kaur, R. P.; Kohli, R. Substituent effect on N-H bond dissociation enthalpies of amines and amides: A theoretical study. *Int. J. Quantum Chem.* **2009**, *109*, 559-568.

73. Sifferlen, T.; Rueping, M.; Gademann, K.; Jaun, B.; Seebach, D. β -Thiopeptides: Synthesis, NMR Solution Structure, CD Spectra, and Photochemistry. *Helv. Chim. Acta* **1999**, *82*, 2067-2093.
74. Bordwell, F. G. Equilibrium acidities in dimethyl sulfoxide solution. *Acc. Chem. Res.* **1988**, *21*, 456-463.
75. Gordon, J. B.; McGale, J. P.; Siegler, M. A.; Goldberg, D. P. Proton-Coupled Electron-Transfer Reactivity Controls Iron versus Sulfur Oxidation in Nonheme Iron–Thiolate Complexes. *Inorg Chem* **2021**, *60*, 6255-6265.
76. Teratani, T.; Koizumi, T.-a.; Yamamoto, T.; Kanbara, T. Changes in redox potential of a nickel-pincer complex bearing reactive secondary thioamide units: Changes caused by deprotonation/protonation reactions on addition of NEt₃ and DBU. *Inorg. Chem. Commun.* **2011**, *14*, 836-838.
77. Okamoto, K.; Yamamoto, T.; Akita, M.; Wada, A.; Kanbara, T. Chemical Stimuli Induced Phosphorescence Modulation of Secondary Thioamide-Based Pincer Platinum Complexes. *Organometallics* **2009**, *28*, 3307-3310.
78. Teratani, T.; Koizumi, T.-a.; Yamamoto, T.; Tanaka, K.; Kanbara, T. Deprotonation/protonation of coordinated secondary thioamide units of pincer ruthenium complexes: Modulation of voltammetric and spectroscopic characterization of the pincer complexes. *Dalton Trans.* **2011**, *40*, 8879-8886.
79. Hickey, D. P.; Cai, R.; Yang, Z.-Y.; Grunau, K.; Einsle, O.; Seefeldt, L. C.; Minter, S. D. Establishing a Thermodynamic Landscape for the Active Site of Mo-Dependent Nitrogenase. *J. Am. Chem. Soc.* **2019**, *141*, 17150-17157.
80. Keutel, H.; Käpplinger, I.; Jäger, E. G.; Grodzicki, M.; Schünemann, V.; Trautwein, A. X. Structural, Magnetic, and Electronic Properties of a Pentacoordinated Intermediate-Spin ($S = 3/2$) Iron(III) Complex with a Macrocyclic [N₄]²⁻ Ligand. *Inorg Chem* **1999**, *38*, 2320-2327.
81. Maier, T. M.; Gawron, M.; Coburger, P.; Bodensteiner, M.; Wolf, R.; van Leest, N. P.; de Bruin, B.; Demeshko, S.; Meyer, F. Low-Valence Anionic α -Diimine Iron Complexes: Synthesis, Characterization, and Catalytic Hydroboration Studies. *Inorg Chem* **2020**, *59*, 16035-16052.

82. Pascualini, M. E.; Stoian, S. A.; Ozarowski, A.; Di Russo, N. V.; Thuijs, A. E.; Abboud, K. A.; Christou, G.; Veige, A. S. Synthesis and characterization of a family of M^{2+} complexes supported by a trianionic ONO^{3-} pincer-type ligand: towards the stabilization of high-spin square-planar complexes. *Dalton Trans.* **2015**, 44, 20207-20215.
83. Roy, N.; Sproules, S.; Bill, E.; Weyhermüller, T.; Wieghardt, K. Molecular and Electronic Structure of the Square Planar Bis(o-amidobenzenethiolato)iron(III) Anion and Its Bis(o-quinoxalinedithiolato)iron(III) Analogue. *Inorg. Chem.* **2008**, 47, 10911-10920.
84. Jain, S. K.; Garg, B. S.; Bhoon, Y. K. Iron(III) complexes of 2-acetylpyridine-4-phenyl-3-thiosemicarbazones: Magnetic, ESR and spectral studies. *Transit. Met. Chem.* **1986**, 11, 89-95.
85. Lugo-Mas, P.; Taylor, W.; Schweitzer, D.; Theisen, R. M.; Xu, L.; Shearer, J.; Swartz, R. D.; Gleaves, M. C.; DiPasquale, A.; Kaminsky, W.; Kovacs, J. A. Properties of Square-Pyramidal Alkyl-Thiolate Fe^{III} Complexes, Including an Analogue of the Unmodified Form of Nitrile Hydratase. *Inorg Chem* **2008**, 47, 11228-11236.
86. Begum, A.; Sarkar, S. An Iron(III) Dithiolene Complex as a Functional Model of Iron Hydrogenase. *Eur. J. Inorg. Chem.* **2012**, 2012, 40-43.
87. Niarchos, D.; Kostikas, A.; Simopoulos, A.; Coucouvanis, D.; Piltingsrud, D.; Coffman, R. E. Mössbauer, magnetic susceptibility, and EPR studies of intermediate spin iron (III) dithiooxalato halides. *J. Chem. Phys.* **1978**, 69, 4411-4418.
88. Fallon, G. D.; Gatehouse, B. M.; Marini, P. J.; Murray, K. S.; West, B. O. Iron complexes of N-substituted thiosalicylideneimines. Part 3. Structure, magnetism, and Mössbauer spectra of the complex chloro[N,N'-ethylenebis(thiosalicylideneiminato)]iron(III), an intermediate-spin complex which exists in three crystalline forms. *J. Chem. Soc., Dalton Trans.* **1984**, 2733-2739.
89. Blume, M. Magnetic Relaxation and Asymmetric Quadrupole Doublets in the Mössbauer Effect. *Phys. Rev. Lett.* **1965**, 14, 96-98.

90. Fataftah, M. S.; Coste, S. C.; Vlaisavljevich, B.; Zadrozny, J. M.; Freedman, D. E. Transformation of the coordination complex $[\text{Co}(\text{C}_3\text{S}_5)_2]^{2-}$ from a molecular magnet to a potential qubit. *Chem. Sci.* **2016**, *7*, 6160-6166.
91. Gatteschi, D.; Sessoli, R. Quantum Tunneling of Magnetization and Related Phenomena in Molecular Materials. *Angew. Chem., Int. Ed.* **2003**, *42*, 268-297.
92. Sanakis, Y.; Power, P. P.; Stubna, A.; Münck, E. Mössbauer Study of the Three-Coordinate Planar Fe^{II} Thiolate Complex $[\text{Fe}(\text{SR})_3]^-$ ($\text{R} = \text{C}_6\text{H}_2\text{-2,4,6-tBu}_3$): Model for the Trigonal Iron Sites of the MoFe_7S_9 :Homocitrate Cofactor of Nitrogenase. *Inorg Chem* **2002**, *41*, 2690-2696.
93. Pascualini, M. E.; Di Russo, N. V.; Thuijs, A. E.; Ozarowski, A.; Stoian, S. A.; Abboud, K. A.; Christou, G.; Veige, A. S. A high-spin square-planar $\text{Fe}(\text{II})$ complex stabilized by a trianionic pincer-type ligand and conclusive evidence for retention of geometry and spin state in solution. *Chem. Sci.* **2015**, *6*, 608-612.
94. Deeth, R. J. Ligand field and density functional descriptions of the d-states and bonding in transition metal complexes. *Faraday Discuss.* **2003**, *124*, 379-391.
95. Kang, K.; Fuller, J.; Reath, A. H.; Ziller, J. W.; Alexandrova, A. N.; Yang, J. Y. Installation of internal electric fields by non-redox active cations in transition metal complexes. *Chem. Sci.* **2019**, *10*, 10135-10142.
96. Chantarojsiri, T.; Reath, A. H.; Yang, J. Y. Cationic Charges Leading to an Inverse Free-Energy Relationship for N–N Bond Formation by Mn^{VI} Nitrides. *Angew. Chem., Int. Ed.* **2018**, *57*, 14037-14042.
97. Chantarojsiri, T.; Ziller, J. W.; Yang, J. Y. Incorporation of redox-inactive cations promotes iron catalyzed aerobic C–H oxidation at mild potentials. *Chem. Sci.* **2018**, *9*, 2567-2574.
98. Dhar, D.; Yee, G. M.; Tolman, W. B. Effects of Charged Ligand Substituents on the Properties of the Formally Copper(III)-Hydroxide ($[\text{CuOH}]^{2+}$) Unit. *Inorg Chem* **2018**, *57*, 9794-9806.
99. Weberg, A. B.; McCollom, S. P.; Thierier, L. M.; Gau, M. R.; Carroll, P. J.; Tomson, N. C. Using internal electrostatic fields to manipulate the valence manifolds of copper complexes. *Chem. Sci.* **2021**, *12*, 4395-4404.

100. Einsle, O.; Tezcan, F. A.; Andrade Susana, L. A.; Schmid, B.; Yoshida, M.; Howard James, B.; Rees Douglas, C. Nitrogenase MoFe-Protein at 1.16 Å Resolution: A Central Ligand in the FeMo-Cofactor. *Science* **2002**, *297*, 1696-1700.
101. Lukoyanov, D.; Yang, Z.-Y.; Barney, B. M.; Dean, D. R.; Seefeldt, L. C.; Hoffman, B. M. Unification of reaction pathway and kinetic scheme for N₂ reduction catalyzed by nitrogenase. *Proc. Natl. Acad. Sci. U.S.A.* **2012**, *109*, 5583.